Spherical signal processing and the Multiverse

Jason McEwen

http://www.jasonmcewen.org/

Department of Physics and Astronomy
University College London (UCL)

IFCA, Universidad de Cantabria :: January 2012

Outline

1. Cosmology
   - Big Bang
   - Cosmic microwave background
   - Observations

2. Harmonic analysis on the sphere
   - Spherical harmonic transform
   - Sampling theorems
   - Comparison

3. Wavelets on the sphere
   - Why wavelets?
   - Continuous wavelets
   - Multiresolution analysis

4. The Multiverse
   - Bubble universes
   - Detection algorithm
   - Candidate bubble collisions in WMAP 7-year observation

Outline

1. Cosmology
   - Big Bang
   - Cosmic microwave background
   - Observations

2. Harmonic analysis on the sphere
   - Spherical harmonic transform
   - Sampling theorems
   - Comparison

3. Wavelets on the sphere
   - Why wavelets?
   - Continuous wavelets
   - Multiresolution analysis

4. The Multiverse
   - Bubble universes
   - Detection algorithm
   - Candidate bubble collisions in WMAP 7-year observation

Cosmological concordance model

- Concordance model of modern cosmology emerged recently with many cosmological parameters constrained to high precision.
- General description is of a Universe undergoing accelerated expansion, containing 4% ordinary baryonic matter, 22% cold dark matter and 74% dark energy.
- Structure and evolution of the Universe constrained through cosmological observations.

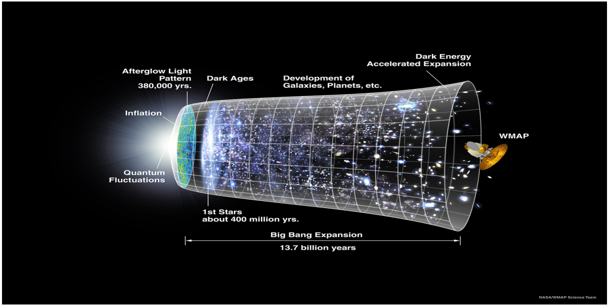

[Credit: WMAP Science Team]

Cosmic microwave background (CMB)

- Temperature of early Universe sufficiently hot that photons had enough energy to ionise hydrogen.
- Compton scattering happened frequently $\Rightarrow$ mean free path of photons extremely small.
- Universe consisted of an opaque photon-baryon fluid.
- As Universe expanded it cooled, until majority of photons no longer had sufficient energy to ionise hydrogen.
- Photons decoupled from baryons and the Universe became essentially transparent to radiation.
- *Recombination* occurred when temperature of Universe dropped to 3000K ($\sim$400,000 years after the Big Bang).
- Photons then free to propagate largely unhindered and observed today on celestial sphere as CMB radiation.
- CMB is highly uniform over the celestial sphere, however it contains small fluctuations at a relative level of 10^{-5} due to acoustic oscillations in the early Universe.
- CMB observed on spherical manifold, hence the geometry of the sphere must be taken into account in any analysis.

Cosmic microwave background (CMB)

- Temperature of early Universe sufficiently hot that photons had enough energy to ionise hydrogen.
- Compton scattering happened frequently $\Rightarrow$ mean free path of photons extremely small.
- Universe consisted of an opaque photon-baryon fluid.
- As Universe expanded it cooled, until majority of photons no longer had sufficient energy to ionise hydrogen.
- Photons decoupled from baryons and the Universe became essentially transparent to radiation.
- *Recombination* occurred when temperature of Universe dropped to 3000K ($\sim$400,000 years after the Big Bang).
- Photons then free to propagate largely unhindered and observed today on celestial sphere as CMB radiation.
- CMB is highly uniform over the celestial sphere, however it contains small fluctuations at a relative level of 10^{-5} due to acoustic oscillations in the early Universe.
- CMB observed on spherical manifold, hence the geometry of the sphere must be taken into account in any analysis.

Cosmic microwave background (CMB)

- Temperature of early Universe sufficiently hot that photons had enough energy to ionise hydrogen.
- Compton scattering happened frequently $\Rightarrow$ mean free path of photons extremely small.
- Universe consisted of an opaque photon-baryon fluid.
- As Universe expanded it cooled, until majority of photons no longer had sufficient energy to ionise hydrogen.
- Photons decoupled from baryons and the Universe became essentially transparent to radiation.
- *Recombination* occurred when temperature of Universe dropped to 3000K ($\sim$400,000 years after the Big Bang).

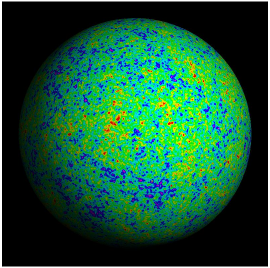

[Credit: Max Tegmark]

- Photons then free to propagate largely unhindered and observed today on celestial sphere as CMB radiation.
- CMB is highly uniform over the celestial sphere, however it contains small fluctuations at a relative level of 10^{-5} due to acoustic oscillations in the early Universe.
- CMB observed on spherical manifold, hence the geometry of the sphere must be taken into account in any analysis.

Cosmic microwave background (CMB)

- Quantum fluctuations in the early Universe blown to macroscopic scales by inflation, establishing acoustic oscillations in primordial plasma of the very early Universe.
- Provide the seeds of structure formation in our Universe.
- Cosmological concordance model explains the power spectrum of these oscillations to very high precision.
- Although a general cosmological concordance model is now established, many details remain unclear. Study of more exotic cosmological models now important.

Cosmic microwave background (CMB)

- Quantum fluctuations in the early Universe blown to macroscopic scales by inflation, establishing acoustic oscillations in primordial plasma of the very early Universe.
- Provide the seeds of structure formation in our Universe.
- Cosmological concordance model explains the power spectrum of these oscillations to very high precision.

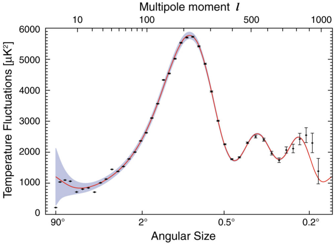

[Credit: WMAP Science Team]

- Although a general cosmological concordance model is now established, many details remain unclear. Study of more exotic cosmological models now important.

Cosmic microwave background (CMB)

- Quantum fluctuations in the early Universe blown to macroscopic scales by inflation, establishing acoustic oscillations in primordial plasma of the very early Universe.
- Provide the seeds of structure formation in our Universe.
- Cosmological concordance model explains the power spectrum of these oscillations to very high precision.

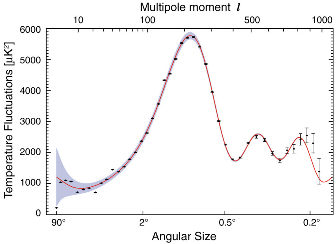

[Credit: WMAP Science Team]

- Although a general cosmological concordance model is now established, many details remain unclear. Study of more exotic cosmological models now important.

Observations of the CMB

- Full-sky observations of the CMB ongoing.

(a) COBE (launched 1989)

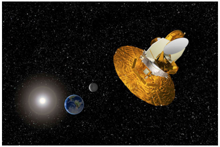

(b) WMAP (launched 2001)

(c) Planck (launched 2009)

- Each new experiment provides dramatic improvement in precision and resolution of observations.

(cobe 2 wmap movie)

(planck movie)

(d) COBE to WMAP [Credit: WMAP Science Team]

(e) Planck observing strategy [Credit: Planck Collaboration]

Outline

Spherical harmonic transform

- The spherical harmonics are the eigenfunctions of the Laplacian on the sphere: $\Delta_{S^2} Y_{\ell m} = -\ell(\ell+1) Y_{\ell m}$.

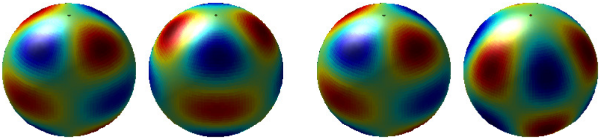

(f) $\ell = 4, m = 2$ (g) $\ell = 4, m = 3$

Figure: Spherical harmonic functions (real and imaginary parts).

- Any square integrable scalar function on the sphere $f \in L^2(S^2)$ may be represented by its spherical harmonic expansion:

$$\boxed{f(\theta,\varphi) = \sum_{\ell=0}^{\infty} \sum_{m=-\ell}^{\ell} f_{\ell m} \, Y_{\ell m}(\theta,\varphi) \, .}$$

- The spherical harmonic coefficients are given by the usual projection onto each basis function:

$$\boxed{f_{\ell m} = \langle f, \, Y_{\ell m} \rangle = \int_{S^2} d\Omega(\theta,\varphi) \, f(\theta,\varphi) \, Y_{\ell m}^*(\theta,\varphi) \, .}$$

- We consider signals on the sphere band-limited at L, that is signals such that $f_{\ell m} = 0, \forall \ell \geq L$.

Spherical harmonic transform

- The spherical harmonics are the eigenfunctions of the Laplacian on the sphere: $\Delta_{\mathbb{S}^2} Y_{\ell m} = -\ell(\ell+1) Y_{\ell m}$.

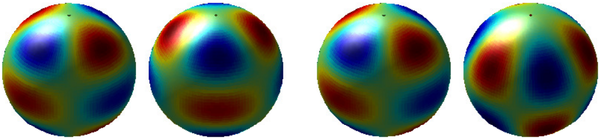

(a) $\ell = 4, m = 2$ (b) $\ell = 4, m = 3$

Figure: Spherical harmonic functions (real and imaginary parts).

- Any square integrable scalar function on the sphere $f \in \mathrm{L}^2(\mathbb{S}^2)$ may be represented by its spherical harmonic expansion:

$$\boxed{f(\theta,\varphi) = \sum_{\ell=0}^{\infty} \sum_{m=-\ell}^{\ell} f_{\ell m} \, Y_{\ell m}(\theta,\varphi) \, .}$$

- The spherical harmonic coefficients are given by the usual projection onto each basis function:

$$\boxed{f_{\ell m} = \langle f, \, Y_{\ell m} \rangle = \int_{\mathbb{S}^2} \mathrm{d}\Omega(\theta,\varphi) \, f(\theta,\varphi) \, Y_{\ell m}^*(\theta,\varphi) \, .}$$

- We consider signals on the sphere band-limited at L, that is signals such that $f_{\ell m} = 0, \, \forall \ell \geq L$.

Sampling theorems on the sphere

- For a band-limited signal, can we compute $f_{\ell m}$ exactly?
  $\rightarrow$ Sampling theorems on the sphere!
- In-exact spherical harmonic transforms exist for a variety of pixelisations of the sphere.
  - `HEALpix` (Gorski *et al.* 2005)
  - `IGLOO` (Crittenden & Turok 1998)

Sampling theorems on the sphere

- For a band-limited signal, can we compute $f_{\ell m}$ exactly?
  $\rightarrow$ Sampling theorems on the sphere!
- In-exact spherical harmonic transforms exist for a variety of pixelisations of the sphere.
  - `HEALpix` (Gorski *et al.* 2005)
  - `IGLOO` (Crittenden & Turok 1998)

Sampling theorems on the sphere

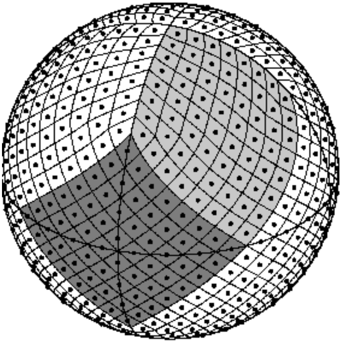

(a) HEALPix [Credit: Gorski *et al.* (2005)]

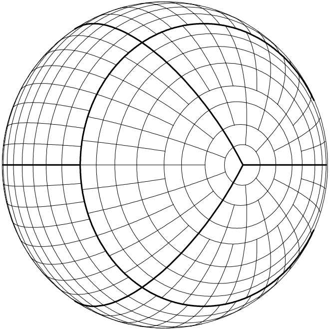

(b) IGLOO [Credit: Crittenden & Turok (2003)]

Figure: Pixelisations of the sphere

Sampling theorems on the sphere

- For a band-limited signal, can we compute $f_{\ell m}$ exactly?
  $\rightarrow$ Sampling theorems on the sphere!
- In-exact spherical harmonic transforms exist for a variety of pixelisations of the sphere.
  - `HEALpix` (Gorski *et al.* 2005)
  - `IGLOO` (Crittenden & Turok 1998)

  $\rightarrow$ Do NOT lead to sampling theorems on the sphere!
- Gauss-Legendre sampling theorem.
- Driscoll & Healy (1994) develop the canonical equiangular sampling theorem on the sphere.

Sampling theorems on the sphere

- For a band-limited signal, can we compute $f_{\ell m}$ exactly?
  $\rightarrow$ Sampling theorems on the sphere!
- In-exact spherical harmonic transforms exist for a variety of pixelisations of the sphere.
  - HEALpix (Gorski *et al.* 2005)
  - IGLOO (Crittenden & Turok 1998)

  $\rightarrow$ Do NOT lead to sampling theorems on the sphere!
- Gauss-Legendre sampling theorem.
- Driscoll & Healy (1994) develop the canonical equiangular sampling theorem on the sphere.

Sampling theorems on the sphere

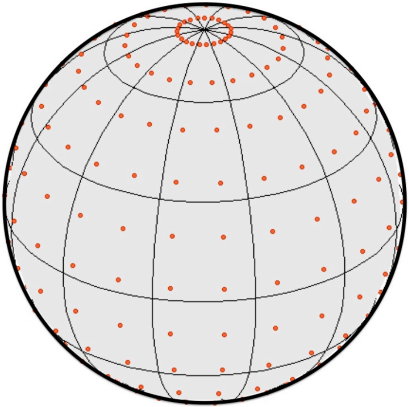

Figure: Equiangular pixelisation of the sphere

Sampling theorems on the sphere

- For a band-limited signal, can we compute $f_{\ell m}$ exactly?
  $\rightarrow$ Sampling theorems on the sphere!
- In-exact spherical harmonic transforms exist for a variety of pixelisations of the sphere.
  - `HEALpix` (Gorski *et al.* 2005)
  - `IGLOO` (Crittenden & Turok 1998)

  $\rightarrow$ Do NOT lead to sampling theorems on the sphere!
- Gauss-Legendre sampling theorem.
- Driscoll & Healy (1994) develop the canonical equiangular sampling theorem on the sphere.
- From an information theoretic viewpoint, fundamental property of any sampling theorem is the number of samples required to capture all of the information of a band-limited signal.
- Develop new equiangular sampling theorem on the sphere with half as many samples as the DH sampling theorem (JDM & Wiaux 2011).

Sampling theorems on the sphere

- For a band-limited signal, can we compute $f_{\ell m}$ exactly?
  $\rightarrow$ Sampling theorems on the sphere!
- In-exact spherical harmonic transforms exist for a variety of pixelisations of the sphere.
  - `HEALpix` (Gorski *et al.* 2005)
  - `IGLOO` (Crittenden & Turok 1998)

  $\rightarrow$ Do NOT lead to sampling theorems on the sphere!
- Gauss-Legendre sampling theorem.
- Driscoll & Healy (1994) develop the canonical equiangular sampling theorem on the sphere.
- From an information theoretic viewpoint, fundamental property of any sampling theorem is the number of samples required to capture all of the information of a band-limited signal.
- Develop new equiangular sampling theorem on the sphere with half as many samples as the DH sampling theorem (JDM & Wiaux 2011).

Sampling theorems on the sphere

- For a band-limited signal, can we compute $f_{\ell m}$ exactly?
  $\rightarrow$ Sampling theorems on the sphere!
- In-exact spherical harmonic transforms exist for a variety of pixelisations of the sphere.
  - `HEALpix` (Gorski *et al.* 2005)
  - `IGLOO` (Crittenden & Turok 1998)

  $\rightarrow$ Do NOT lead to sampling theorems on the sphere!
- Gauss-Legendre sampling theorem.
- Driscoll & Healy (1994) develop the canonical equiangular sampling theorem on the sphere.
- From an information theoretic viewpoint, fundamental property of any sampling theorem is the number of samples required to capture all of the information of a band-limited signal.
- Develop new equiangular sampling theorem on the sphere with half as many samples as the DH sampling theorem (JDM & Wiaux 2011).

A novel sampling theorem

- We have developed a new sampling theorem and corresponding fast algorithms by performing a factoring of rotations and then by associating the sphere with the torus through a periodic extension.
- Similar (in flavour but not detail!) to making a periodic extension in θ of a function f on the sphere.

A novel sampling theorem

- We have developed a new sampling theorem and corresponding fast algorithms by performing a factoring of rotations and then by associating the sphere with the torus through a periodic extension.
- Similar (in flavour but not detail!) to making a periodic extension in θ of a function f on the sphere.

(a) Function on sphere (b) Even function on torus (c) Odd function on torus

Figure: Associating functions on the sphere and torus

A novel sampling theorem

- By a factoring of rotations (Wigner decomposition), a reordering of summations and a separation of variables, the inverse transform of ${}_sf$ may be written:

Inverse spherical harmonic transform

$$ {}_sf(\theta,\varphi) = \sum_{m=-(L-1)}^{L-1} {}_sF_m(\theta)\, \mathrm{e}^{\mathrm{i}m\varphi} $$

$$ {}_sF_m(\theta) = \sum_{m'=-(L-1)}^{L-1} {}_sF_{mm'}\, \mathrm{e}^{\mathrm{i}m'\theta} $$

$$ {}_sF_{mm'} = (-1)^s\, \mathrm{i}^{-(m+s)} \sum_{\ell=0}^{L-1} \sqrt{\frac{2\ell+1}{4\pi}}\, \Delta^\ell_{m'm}\, \Delta^\ell_{m',-s}\, {}_sf_{\ell m} $$

where $\Delta^\ell_{mn} \equiv d^\ell_{mn}(\pi/2)$ are the reduced Wigner functions evaluated at $\pi/2$.

A novel sampling theorem

- By a factoring of rotations (Wigner decomposition), a reordering of summations and a separation of variables, the forward transform of ${}_sf$ may be written:

Forward spherical harmonic transform

$$
{}_sf_{\ell m} = (-1)^s \, \mathrm{i}^{m+s} \sqrt{\frac{2\ell+1}{4\pi}} \sum_{m'=-(L-1)}^{L-1} \Delta^{\ell}_{m' m} \, \Delta^{\ell}_{m', -s} \; {}_sG_{mm'}
$$

$$
{}_sG_{mm'} = \int_0^{\pi} \mathrm{d}\theta \sin\theta \; {}_sG_m(\theta) \, \mathrm{e}^{-\mathrm{i}m'\theta}
$$

$$
{}_sG_m(\theta) = \int_0^{2\pi} \mathrm{d}\varphi \; {}_sf(\theta,\varphi) \, \mathrm{e}^{-\mathrm{i}m\varphi}
$$

- Recasting the forward and inverse spherical harmonic transforms in this manner is no more efficient or accurate than the original formulation.
- However, it highlights similarities with Fourier series representations and reduces the problem of finding an exact quadrature rule to the calculation of ${}_sG_{mm'}$ only.
- The Fourier series expansion is only defined for periodic functions; thus, to recast these expressions in a form amenable to the application of Fourier transforms we must make a periodic extension in colatitude θ.

A novel sampling theorem

- By a factoring of rotations (Wigner decomposition), a reordering of summations and a separation of variables, the forward transform of ${}_sf$ may be written:

Forward spherical harmonic transform

$$
{}_sf_{\ell m} = (-1)^s \, \mathrm{i}^{m+s} \sqrt{\frac{2\ell+1}{4\pi}} \sum_{m'=-(L-1)}^{L-1} \Delta^{\ell}_{m' m} \, \Delta^{\ell}_{m',-s} \; {}_sG_{mm'}
$$

$$
{}_sG_{mm'} = \int_0^{\pi} \mathrm{d}\theta \sin\theta \; {}_sG_m(\theta) \, \mathrm{e}^{-\mathrm{i}m'\theta}
$$

$$
{}_sG_m(\theta) = \int_0^{2\pi} \mathrm{d}\varphi \; {}_sf(\theta,\varphi) \, \mathrm{e}^{-\mathrm{i}m\varphi}
$$

- Recasting the forward and inverse spherical harmonic transforms in this manner is no more efficient or accurate than the original formulation.
- However, it highlights similarities with Fourier series representations and reduces the problem of finding an exact quadrature rule to the calculation of ${}_sG_{mm'}$ only.
- The Fourier series expansion is only defined for periodic functions; thus, to recast these expressions in a form amenable to the application of Fourier transforms we must make a periodic extension in colatitude θ.

Comparison

	DH Divide-and-conquer	DH Semi-naive	MW
Pixelisation scheme	equiangular	equiangular	equiangular
Asymptotic complexity	$\mathcal{O}(L^{5/2} \log_2^{1/2} L)$	$\mathcal{O}(L^3)$	$\mathcal{O}(L^3)$
Precomputation	Y	N	N
Stability	N	Y	Y
Flexibility of Wigner recursion	N	N	Y
Number of samples	$\mathbf{4L^2}$	$\mathbf{4L^2}$	$\mathbf{2L^2}$

Comparison

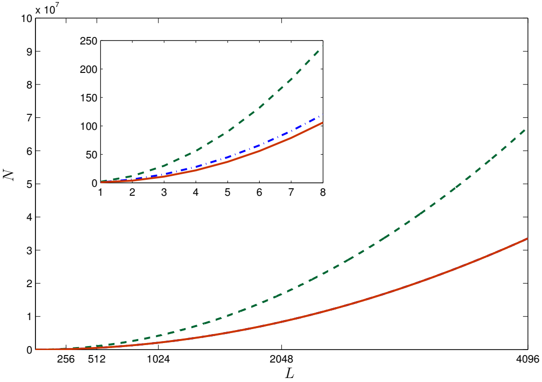

Figure: Number of samples (MW=red; DH=green; GL=blue)

Comparison

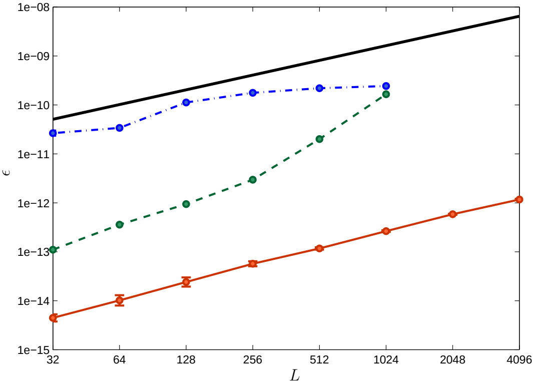

Figure: Numerical accuracy (MW=red; DH=green; GL=blue)

Comparison

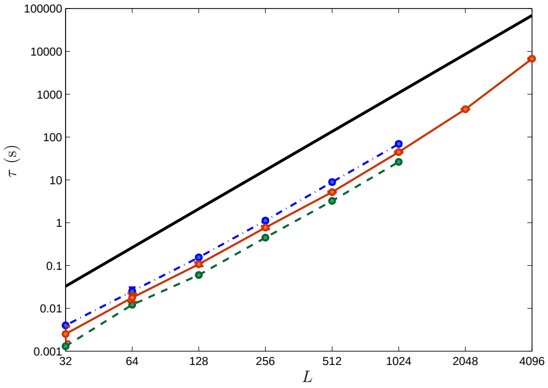

Figure: Computation time (MW=red; DH=green; GL=blue)

Outline

Why wavelets?

Fourier (1807)

Haar (1909)

Morlet and Grossman (1981)

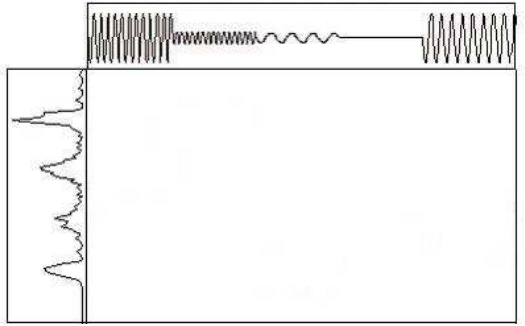

Figure: Fourier vs wavelet transform (image from `http://www.wavelet.org/tutorial/`)

Why wavelets?

Fourier (1807)

Haar (1909)

Morlet and Grossman (1981)

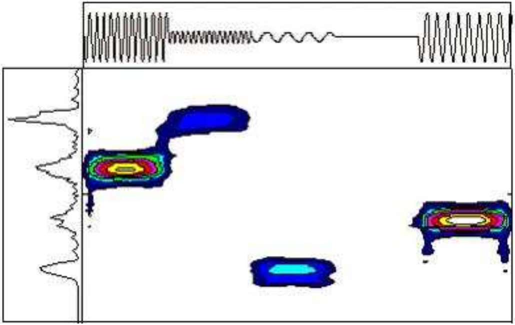

Figure: Fourier vs wavelet transform (image from `http://www.wavelet.org/tutorial/`)

Wavelet transform in Euclidean space

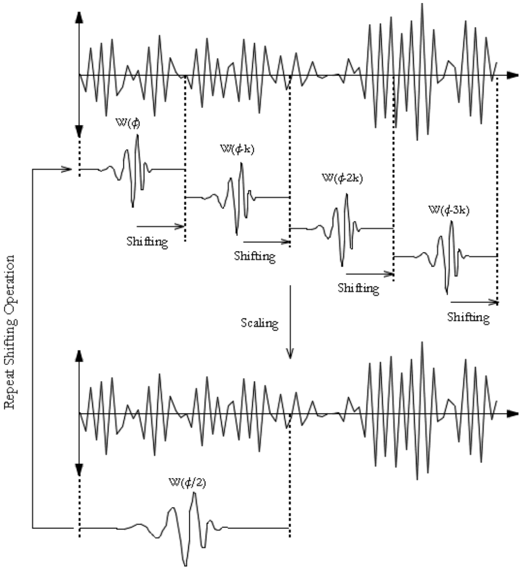

Figure: Wavelet scaling and shifting (image from `http://www.wavelet.org/tutorial/`)

Wavelet transform in Euclidean space

- Project signal onto wavelets

$$\mathcal{W}^f(a,b) = \langle f, \psi_{a,b} \rangle = |a|^{-1/2} \int_{-\infty}^{\infty} \mathrm{d}t\, f(t)\, \psi^* \left(\frac{t-b}{a} \right),$$

where $\psi_{a,b} = |a|^{-1/2} \psi(\frac{t-b}{a})$.

- Synthesis signal from wavelet coefficients

$$f(t) = C_\psi^{-1} \int_{-\infty}^{\infty} \mathrm{d}b \int_0^{\infty} \frac{\mathrm{d}a}{a^2}\, \mathcal{W}^f(a,b) \psi_{a,b}(t).$$

- Admissibility condition to ensure perfect reconstruction

$$0 < C_\psi \equiv \int_{-\infty}^{\infty} \frac{\mathrm{d}k}{|k|} |\hat{\psi}(k)|^2 < \infty.$$

- Construct on sphere in analogous manner.

Wavelets on the sphere

- Follow construction derived by Antoine and Vandergheynst (1998) (reintroduced by Wiaux (2005)).
- Construct wavelet atoms from affine transformations (dilation, translation) on the sphere of a mother wavelet.
- The natural extension of translations to the sphere are rotations. Characterised by the elements of the rotation group $\mathrm{SO}(3)$, which parameterise in terms of the three Euler angles $\rho = (\alpha, \beta, \gamma)$. Rotation of a function f on the sphere is defined by

$$[\mathcal{R}(\rho)f](\omega) = f(\rho^{-1}\omega), \quad \rho \in \mathrm{SO}(3) .$$

- How define dilation and admissible wavelets on the sphere?

Wavelets on the sphere

- Follow construction derived by Antoine and Vandergheynst (1998)
  (reintroduced by Wiaux (2005)).
- Construct wavelet atoms from affine transformations (dilation, translation) on the sphere of a mother wavelet.
- The natural extension of translations to the sphere are rotations. Characterised by the elements of the rotation group $\mathrm{SO}(3)$, which parameterise in terms of the three Euler angles $\rho = (\alpha, \beta, \gamma)$. Rotation of a function f on the sphere is defined by

$$[\mathcal{R}(\rho) f](\omega) = f(\rho^{-1}\omega), \quad \rho \in \mathrm{SO}(3) \; .$$

- How define dilation and admissible wavelets on the sphere?

Wavelets on the sphere

- Follow construction derived by Antoine and Vandergheynst (1998)
  (reintroduced by Wiaux (2005)).
- Construct wavelet atoms from affine transformations (dilation, translation) on the sphere of a mother wavelet.
- The natural extension of translations to the sphere are rotations. Characterised by the elements of the rotation group $\mathrm{SO}(3)$, which parameterise in terms of the three Euler angles $\rho = (\alpha, \beta, \gamma)$. Rotation of a function f on the sphere is defined by

$$[\mathcal{R}(\rho)f](\omega) = f(\rho^{-1}\omega), \quad \rho \in \mathrm{SO}(3) \ .$$

- How define dilation and admissible wavelets on the sphere?

Stereographic projection

- Apply stereographic projection to build an association with the plane.

- Stereographic projection operator is defined by $\Pi : \omega \rightarrow \boldsymbol{x} = \Pi\omega = (r(\theta), \varphi)$ where $r = 2\tan(\theta/2)$, $\omega \equiv (\theta, \varphi) \in \mathrm{S}^2$ and $\boldsymbol{x} \in \mathbb{R}^2$ is a point in the plane, denoted here by the polar coordinates (r, φ). The inverse operator is $\Pi^{-1} : \boldsymbol{x} \rightarrow \omega = \Pi^{-1}\boldsymbol{x} = (\theta(r), \varphi)$, where $\theta(r) = 2\tan^{-1}(r/2)$.

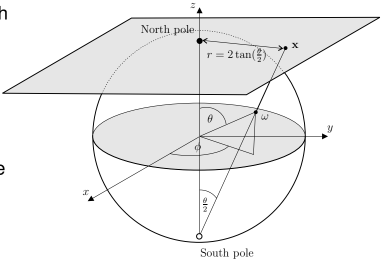

- Define the action of the stereographic projection operator on functions on the plane and sphere. Consider the space of square integrable functions in $\mathrm{L}^2(\mathbb{R}^2, \mathrm{d}^2\boldsymbol{x})$ on the plane and $\mathrm{L}^2(\mathrm{S}^2, \mathrm{d}\Omega(\omega))$ on the sphere.
  - The action of the stereographic projection operator $\Pi : f \in \mathrm{L}^2(\mathrm{S}^2, \mathrm{d}\Omega(\omega)) \rightarrow p = \Pi f \in \mathrm{L}^2(\mathbb{R}^2, \mathrm{d}^2\boldsymbol{x})$ on functions is defined as

$$p(r, \varphi) = (\Pi f)(r, \varphi) = (1 + r^2/4)^{-1} f(\theta(r), \varphi) .$$

  - The inverse stereographic projection operator $\Pi^{-1} : p \in \mathrm{L}^2(\mathbb{R}^2, \mathrm{d}^2\boldsymbol{x}) \rightarrow f = \Pi^{-1} p \in \mathrm{L}^2(\mathrm{S}^2, \mathrm{d}\Omega(\omega))$ on functions is then

$$f(\theta, \varphi) = (\Pi^{-1} p)(\theta, \varphi) = [1 + \tan^2(\theta/2)] p(r(\theta), \varphi) .$$

Stereographic projection

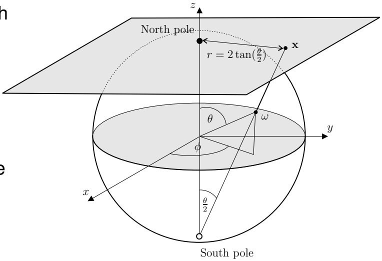

- Apply stereographic projection to build an association with the plane.
- Stereographic projection operator is defined by $\Pi : \omega \rightarrow \boldsymbol{x} = \Pi\omega = (r(\theta), \varphi)$ where $r = 2\tan(\theta/2)$, $\omega \equiv (\theta, \varphi) \in \mathrm{S}^2$ and $\boldsymbol{x} \in \mathbb{R}^2$ is a point in the plane, denoted here by the polar coordinates (r, φ). The inverse operator is $\Pi^{-1} : \boldsymbol{x} \rightarrow \omega = \Pi^{-1}\boldsymbol{x} = (\theta(r), \varphi)$, where $\theta(r) = 2\tan^{-1}(r/2)$.
- Define the action of the stereographic projection operator on functions on the plane and sphere. Consider the space of square integrable functions in $\mathrm{L}^2(\mathbb{R}^2, \mathrm{d}^2\boldsymbol{x})$ on the plane and $\mathrm{L}^2(\mathrm{S}^2, \mathrm{d}\Omega(\omega))$ on the sphere.
  - The action of the stereographic projection operator $\Pi : f \in \mathrm{L}^2(\mathrm{S}^2, \mathrm{d}\Omega(\omega)) \rightarrow p = \Pi f \in \mathrm{L}^2(\mathbb{R}^2, \mathrm{d}^2\boldsymbol{x})$ on functions is defined as

$$p(r, \varphi) = (\Pi f)(r, \varphi) = (1 + r^2/4)^{-1} f(\theta(r), \varphi) \; .$$

  - The inverse stereographic projection operator $\Pi^{-1} : p \in \mathrm{L}^2(\mathbb{R}^2, \mathrm{d}^2\boldsymbol{x}) \rightarrow f = \Pi^{-1}p \in \mathrm{L}^2(\mathrm{S}^2, \mathrm{d}\Omega(\omega))$ on functions is then

$$f(\theta, \varphi) = (\Pi^{-1}p)(\theta, \varphi) = [1 + \tan^2(\theta/2)]p(r(\theta), \varphi) \; .$$

Dilation on the sphere

- The spherical dilation operator $\mathcal{D}(a) : f(\omega) \rightarrow [\mathcal{D}(a)f](\omega)$ in $\mathrm{L}^2(\mathrm{S}^2, \mathrm{d}\Omega(\omega))$ is defined as the conjugation by Π of the Euclidean dilation $d(a)$ in $\mathrm{L}^2(\mathbb{R}^2, \mathrm{d}^2\boldsymbol{x})$ on tangent plane at north pole:

$$\mathcal{D}(a) \equiv \Pi^{-1}\, d(a)\, \Pi \, .$$

- Spherical dilation given by

$$[\mathcal{D}(a)f](\omega) = [\lambda(a, \theta, \varphi)]^{1/2} f(\omega_{1/a}) \, ,$$

where $\omega_a = (\theta_a, \varphi)$ and $\tan(\theta_a/2) = a \tan(\theta/2)$.

- Cocycle of a spherical dilation is defined by

$$\lambda(a, \theta, \varphi) \equiv \frac{4a^2}{[(a^2 - 1)\cos\theta + (a^2 + 1)]^2} \, .$$

Wavelet analysis

- Wavelets on the sphere may now be constructed from rotations and dilations of a mother spherical wavelet $\Phi \in \mathrm{L}^2(\mathrm{S}^2, \mathrm{d}\Omega(\omega))$. The corresponding wavelet family $\{\Phi_{a,\rho} \equiv \mathcal{R}(\rho)\mathcal{D}(a)\Phi : \rho \in \mathrm{SO}(3), a \in \mathbb{R}_*^+\}$ provides an over-complete set of functions in $\mathrm{L}^2(\mathrm{S}^2, \mathrm{d}\Omega(\omega))$.
- The CSWT of $f \in \mathrm{L}^2(\mathrm{S}^2, \mathrm{d}\Omega(\omega))$ is given by the projection on to each wavelet atom in the usual manner:

$$\boxed{\widehat{\mathcal{W}}_\Phi^f(a, \rho) = \langle f, \Phi_{a,\rho} \rangle = \int_{\mathrm{S}^2} \mathrm{d}\Omega(\omega)\, f(\omega)\, \Phi_{a,\rho}^*(\omega)\,,}$$

  where $\mathrm{d}\Omega(\omega) = \sin\theta\, \mathrm{d}\theta\, \mathrm{d}\varphi$ is the usual invariant measure on the sphere.
- Transform general in the sense that all orientations in the rotation group $\mathrm{SO}(3)$ are considered, thus directional structure is naturally incorporated.
- Fast algorithms essential (for a review see Wiaux, JDM *et al.* 2007)
  - Factoring of rotations: JDM *et al.* (2007)
  - Separation of variables: Wiaux *et al.* (2005)

Wavelet analysis

- Wavelets on the sphere may now be constructed from rotations and dilations of a mother spherical wavelet $\Phi \in \mathrm{L}^2(\mathrm{S}^2, \, \mathrm{d}\Omega(\omega))$. The corresponding wavelet family $\{\Phi_{a,\rho} \equiv \mathcal{R}(\rho)\mathcal{D}(a)\Phi \, : \, \rho \in \mathrm{SO}(3), \, a \in \mathbb{R}_*^+\}$ provides an over-complete set of functions in $\mathrm{L}^2(\mathrm{S}^2, \, \mathrm{d}\Omega(\omega))$.

- The CSWT of $f \in \mathrm{L}^2(\mathrm{S}^2, \, \mathrm{d}\Omega(\omega))$ is given by the projection on to each wavelet atom in the usual manner:

$$\boxed{\widehat{\mathcal{W}}_{\Phi}^{f}(a, \rho) = \langle f, \Phi_{a,\rho} \rangle = \int_{\mathrm{S}^2} \mathrm{d}\Omega(\omega) \, f(\omega) \, \Phi_{a,\rho}^{*}(\omega) \; ,}$$

  where $\mathrm{d}\Omega(\omega) = \sin\theta \, \mathrm{d}\theta \, \mathrm{d}\varphi$ is the usual invariant measure on the sphere.

- Transform general in the sense that all orientations in the rotation group $\mathrm{SO}(3)$ are considered, thus directional structure is naturally incorporated.

- Fast algorithms essential (for a review see Wiaux, JDM *et al.* 2007)
  - Factoring of rotations: JDM *et al.* (2007)
  - Separation of variables: Wiaux *et al.* (2005)

Wavelet analysis

- Wavelets on the sphere may now be constructed from rotations and dilations of a mother spherical wavelet $\Phi \in \mathrm{L}^2(\mathrm{S}^2, \, \mathrm{d}\Omega(\omega))$. The corresponding wavelet family $\{\Phi_{a,\rho} \equiv \mathcal{R}(\rho)\mathcal{D}(a)\Phi \, : \, \rho \in \mathrm{SO}(3), \, a \in \mathbb{R}_*^+\}$ provides an over-complete set of functions in $\mathrm{L}^2(\mathrm{S}^2, \, \mathrm{d}\Omega(\omega))$.
- The CSWT of $f \in \mathrm{L}^2(\mathrm{S}^2, \, \mathrm{d}\Omega(\omega))$ is given by the projection on to each wavelet atom in the usual manner:

$$\boxed{\widehat{\mathcal{W}}_\Phi^f(a, \rho) = \langle f, \Phi_{a,\rho} \rangle = \int_{\mathrm{S}^2} \mathrm{d}\Omega(\omega) \, f(\omega) \, \Phi_{a,\rho}^*(\omega) \, ,}$$

  where $\mathrm{d}\Omega(\omega) = \sin\theta \, \mathrm{d}\theta \, \mathrm{d}\varphi$ is the usual invariant measure on the sphere.
- Transform general in the sense that all orientations in the rotation group $\mathrm{SO}(3)$ are considered, thus directional structure is naturally incorporated.
- Fast algorithms essential (for a review see Wiaux, JDM *et al.* 2007)
  - Factoring of rotations: JDM *et al.* (2007)
  - Separation of variables: Wiaux *et al.* (2005)

Wavelet synthesis

- The synthesis of a signal on the sphere from its wavelet coefficients is given by

$$\boxed{f(\omega) = \int_0^{\infty} \frac{\mathrm{d}a}{a^3} \int_{\mathrm{SO}(3)} \mathrm{d}\varrho(\rho) \widehat{\mathcal{W}}_{\Phi}^{f}(a, \rho) \, [\mathcal{R}(\rho)\widehat{L}_{\Phi}\Phi_a](\omega) \ ,}$$

  where $\mathrm{d}\varrho(\rho) = \sin\beta \, \mathrm{d}\alpha \, \mathrm{d}\beta \, \mathrm{d}\gamma$ is the invariant measure on the rotation group $\mathrm{SO}(3)$.

- The $\widehat{L}_{\Phi}$ operator in $\mathrm{L}^2(\mathrm{S}^2, \mathrm{d}\Omega(\omega))$ is defined by the action

$$(\widehat{L}_{\Phi} g)_{\ell m} \equiv g_{\ell m} / \widehat{C}_{\Phi}^{\ell}$$

  on the spherical harmonic coefficients of functions $g \in \mathrm{L}^2(\mathrm{S}^2, \mathrm{d}\Omega(\omega))$.

- In order to ensure the perfect reconstruction of a signal synthesised from its wavelet coefficients, the admissibility condition

$$\boxed{0 < \widehat{C}_{\Phi}^{\ell} \equiv \frac{8\pi^2}{2\ell+1} \sum_{m=-\ell}^{\ell} \int_0^{\infty} \frac{\mathrm{d}a}{a^3} \mid (\Phi_a)_{\ell m} \mid^2 < \infty}$$

  must be satisfied for all $\ell \in \mathbb{N}$, where $(\Phi_a)_{\ell m}$ are the spherical harmonic coefficients of $\Phi_a(\omega)$.

Wavelet synthesis

- The synthesis of a signal on the sphere from its wavelet coefficients is given by

$$\boxed{f(\omega) = \int_0^\infty \frac{\mathrm{d}a}{a^3} \int_{\mathrm{SO}(3)} \mathrm{d}\varrho(\rho) \widehat{\mathcal{W}}_\Phi^f(a,\rho)\, [\mathcal{R}(\rho)\widehat{L}_\Phi \Phi_a](\omega)\ ,}$$

where $\mathrm{d}\varrho(\rho) = \sin\beta\,\mathrm{d}\alpha\,\mathrm{d}\beta\,\mathrm{d}\gamma$ is the invariant measure on the rotation group $\mathrm{SO}(3)$.

- The $\widehat{L}_\Phi$ operator in $\mathrm{L}^2(\mathrm{S}^2,\ \mathrm{d}\Omega(\omega))$ is defined by the action

$$(\widehat{L}_\Phi g)_{\ell m} \equiv g_{\ell m} / \widehat{C}_\Phi^\ell$$

on the spherical harmonic coefficients of functions $g \in \mathrm{L}^2(\mathrm{S}^2,\ \mathrm{d}\Omega(\omega))$.

- In order to ensure the perfect reconstruction of a signal synthesised from its wavelet coefficients, the admissibility condition

$$\boxed{0 < \widehat{C}_\Phi^\ell \equiv \frac{8\pi^2}{2\ell+1} \sum_{m=-\ell}^{\ell} \int_0^\infty \frac{\mathrm{d}a}{a^3} \mid (\Phi_a)_{\ell m} \mid^2 < \infty}$$

must be satisfied for all $\ell \in \mathbb{N}$, where $(\Phi_a)_{\ell m}$ are the spherical harmonic coefficients of $\Phi_a(\omega)$.

Correspondence principle

- Correspondence principle between spherical and Euclidean wavelets states that the inverse stereographic projection of an *admissible* wavelet on the plane yields an *admissible* wavelet on the sphere (proved by Wiaux *et al.* 2005)
- Mother wavelets on sphere constructed from the projection of mother Euclidean wavelets defined on the plane:

$$\Phi = \Pi^{-1} \Phi_{\mathbb{R}^2} ,$$

where $\Phi_{\mathbb{R}^2} \in \mathrm{L}^2(\mathbb{R}^2, \mathrm{d}^2\boldsymbol{x})$ is an admissible wavelet in the plane.
- Directional wavelets on sphere may be naturally constructed in this setting – they are simply the projection of directional Euclidean planar wavelets on to the sphere.

Correspondence principle

- Correspondence principle between spherical and Euclidean wavelets states that the inverse stereographic projection of an *admissible* wavelet on the plane yields an *admissible* wavelet on the sphere (proved by Wiaux *et al.* 2005)
- Mother wavelets on sphere constructed from the projection of mother Euclidean wavelets defined on the plane:

$$\Phi = \Pi^{-1}\Phi_{\mathbb{R}^2} \ ,$$

  where $\Phi_{\mathbb{R}^2} \in \mathrm{L}^2(\mathbb{R}^2,\ \mathrm{d}^2\boldsymbol{x})$ is an admissible wavelet in the plane.
- Directional wavelets on sphere may be naturally constructed in this setting – they are simply the projection of directional Euclidean planar wavelets on to the sphere.

Correspondence principle

- Correspondence principle between spherical and Euclidean wavelets states that the inverse stereographic projection of an *admissible* wavelet on the plane yields an *admissible* wavelet on the sphere (proved by Wiaux *et al.* 2005)
- Mother wavelets on sphere constructed from the projection of mother Euclidean wavelets defined on the plane:

$$\Phi = \Pi^{-1}\Phi_{\mathbb{R}^2} \ ,$$

  where $\Phi_{\mathbb{R}^2} \in \mathrm{L}^2(\mathbb{R}^2,\ \mathrm{d}^2\boldsymbol{x})$ is an admissible wavelet in the plane.
- Directional wavelets on sphere may be naturally constructed in this setting – they are simply the projection of directional Euclidean planar wavelets on to the sphere.

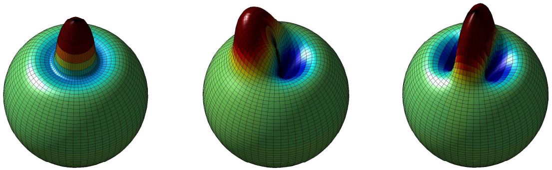

(a) SMHW (b) SBW (c) S2GDW

Figure: Spherical wavelets at scale $a, b = 0.2$.

Multiresolution analysis on the sphere

- Define multiresolution analysis on the sphere in an analogous manner to Euclidean framework.
- Define approximation spaces on the sphere $V_j \subset \mathrm{L}^2(\mathrm{S}^2)$
- Construct the nested hierarchy of approximation spaces

$$V_1 \subset V_2 \subset \cdots \subset V_J \subset \mathrm{L}^2(\mathrm{S}^2) ,$$

where coarser (finer) approximation spaces correspond to a lower (higher) resolution level j.

- For each space V_j we define a basis with basis elements given by the *scaling functions* $\varphi_{j,k} \in V_j$, where the k index corresponds to a translation on the sphere.
- Define detail space W_j to be the orthogonal complement of V_j in V_{j+1}, *i.e.* $V_{j+1} = V_j \oplus W_j$.
- For each space W_j we define a basis with basis elements given by the *wavelets* $\psi_{j,k} \in W_j$.
- Expanding the hierarchy of approximation spaces:

$$V_J = V_1 \oplus \bigoplus_{j=1}^{J-1} W_j .$$

Multiresolution analysis on the sphere

- Define multiresolution analysis on the sphere in an analogous manner to Euclidean framework.
- Define approximation spaces on the sphere $V_j \subset \mathrm{L}^2(\mathrm{S}^2)$
- Construct the nested hierarchy of approximation spaces

$$V_1 \subset V_2 \subset \cdots \subset V_J \subset \mathrm{L}^2(\mathrm{S}^2) ,$$

  where coarser (finer) approximation spaces correspond to a lower (higher) resolution level j.
- For each space V_j we define a basis with basis elements given by the *scaling functions* $\varphi_{j,k} \in V_j$, where the k index corresponds to a translation on the sphere.
- Define detail space W_j to be the orthogonal complement of V_j in V_{j+1}, *i.e.* $V_{j+1} = V_j \oplus W_j$.
- For each space W_j we define a basis with basis elements given by the *wavelets* $\psi_{j,k} \in W_j$.
- Expanding the hierarchy of approximation spaces:

$$V_J = V_1 \oplus \bigoplus_{j=1}^{J-1} W_j .$$

Multiresolution analysis on the sphere

- Define multiresolution analysis on the sphere in an analogous manner to Euclidean framework.
- Define approximation spaces on the sphere $V_j \subset \mathrm{L}^2(\mathrm{S}^2)$
- Construct the nested hierarchy of approximation spaces

$$V_1 \subset V_2 \subset \cdots \subset V_J \subset \mathrm{L}^2(\mathrm{S}^2) \, ,$$

 where coarser (finer) approximation spaces correspond to a lower (higher) resolution level j.

- For each space V_j we define a basis with basis elements given by the *scaling functions* $\varphi_{j,k} \in V_j$, where the k index corresponds to a translation on the sphere.
- Define detail space W_j to be the orthogonal complement of V_j in V_{j+1}, *i.e.* $V_{j+1} = V_j \oplus W_j$.
- For each space W_j we define a basis with basis elements given by the *wavelets* $\psi_{j,k} \in W_j$.
- Expanding the hierarchy of approximation spaces:

$$V_J = V_1 \oplus \bigoplus_{j=1}^{J-1} W_j \, .$$

Hierarchical pixelisation of the sphere

- Relate generic multiresolution decomposition to `HEALPix` hierarchical pixelisation of the sphere.
- Haar wavelets on the sphere first constructed in this manner by Barreiro *et al.* (2000).

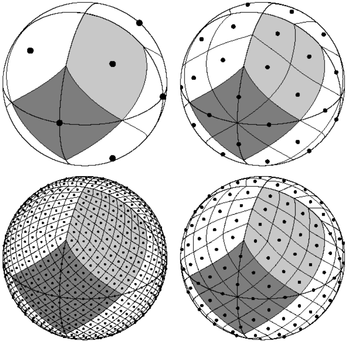

[Credit: Gorski *et al.* (2005)]

Haar wavelets on the sphere

- Let V_j correspond to a `HEALPix` pixelised sphere with resolution parameter $N_{\text{side}} = 2^{j-1}$.
- Define the scaling function $\varphi_{j,k}$ at level j to be constant for pixel k and zero elsewhere:

$$\varphi_{j,k}(\omega) \equiv \begin{cases} 1/\sqrt{A_j} & \omega \in P_{j,k} \\ 0 & \text{elsewhere}\ . \end{cases}$$

- Orthonormal basis for the wavelet space W_j given by the following wavelets:

$$\psi^0_{j,k}(\omega) \equiv \left[\varphi_{j+1,k_0}(\omega) - \varphi_{j+1,k_1}(\omega) + \varphi_{j+1,k_2}(\omega) - \varphi_{j+1,k_3}(\omega)\right]/2\ ;$$

$$\psi^1_{j,k}(\omega) \equiv \left[\varphi_{j+1,k_0}(\omega) + \varphi_{j+1,k_1}(\omega) - \varphi_{j+1,k_2}(\omega) - \varphi_{j+1,k_3}(\omega)\right]/2\ ;$$

$$\psi^2_{j,k}(\omega) \equiv \left[\varphi_{j+1,k_0}(\omega) - \varphi_{j+1,k_1}(\omega) - \varphi_{j+1,k_2}(\omega) + \varphi_{j+1,k_3}(\omega)\right]/2\ .$$

Haar wavelets on the sphere

- Let V_j correspond to a HEALPix pixelised sphere with resolution parameter $N_{\text{side}} = 2^{j-1}$.
- Define the scaling function $\varphi_{j,k}$ at level j to be constant for pixel k and zero elsewhere:

$$\varphi_{j,k}(\omega) \equiv \begin{cases} 1/\sqrt{A_j} & \omega \in P_{j,k} \\ 0 & \text{elsewhere} . \end{cases}$$

- Orthonormal basis for the wavelet space W_j given by the following wavelets:

$$\psi^0_{j,k}(\omega) \equiv \left[\varphi_{j+1,k_0}(\omega) - \varphi_{j+1,k_1}(\omega) + \varphi_{j+1,k_2}(\omega) - \varphi_{j+1,k_3}(\omega)\right]/2 \, ;$$
$$\psi^1_{j,k}(\omega) \equiv \left[\varphi_{j+1,k_0}(\omega) + \varphi_{j+1,k_1}(\omega) - \varphi_{j+1,k_2}(\omega) - \varphi_{j+1,k_3}(\omega)\right]/2 \, ;$$
$$\psi^2_{j,k}(\omega) \equiv \left[\varphi_{j+1,k_0}(\omega) - \varphi_{j+1,k_1}(\omega) - \varphi_{j+1,k_2}(\omega) + \varphi_{j+1,k_3}(\omega)\right]/2 \, .$$

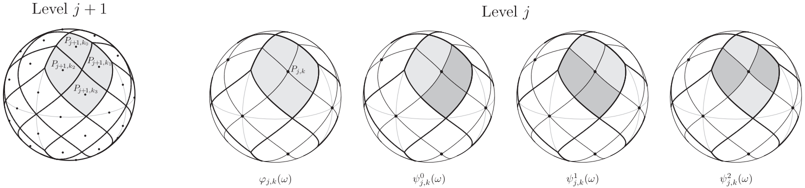

Figure: Haar scaling function $\varphi_{j,k}(\omega)$ and wavelets $\psi^m_{j,k}(\omega)$

Haar wavelets on the sphere

- Multiresolution decomposition of a function defined on a `HEALPix` data-sphere at resolution J, *i.e.* $f_J \in V_J$ proceeds as follows.
- Approximation coefficients at the coarser level j are given by the projection of f_{j+1} onto the scaling functions $\varphi_{j,k}$:

$$\lambda_{j,k} = \int_{S^2} f_{j+1}(\omega)\ \varphi_{j,k}(\omega)\ \mathrm{d}\Omega\ .$$

- Detail coefficients at level j are given by the projection of f_{j+1} onto the wavelets $\psi^m_{j,k}$:

$$\gamma^m_{j,k} = \int_{S^2} f_{j+1}(\omega)\ \psi^m_{j,k}(\omega)\ \mathrm{d}\Omega\ .$$

- The function $f_J \in V_J$ may then be synthesised from its approximation and detail coefficients:

$$f_J(\omega) = \sum_{k=0}^{N_{J_0}-1} \lambda_{J_0 k}\varphi_{J_0 k}(\omega) + \sum_{j=J_0}^{J-1}\sum_{k=0}^{N_j-1}\sum_{m=0}^{2} \gamma^m_{j,k}\psi^m_{j,k}(\omega)\ .$$

Haar wavelets on the sphere

- Multiresolution decomposition of a function defined on a HEALPix data-sphere at resolution J, *i.e.* $f_J \in V_J$ proceeds as follows.
- Approximation coefficients at the coarser level j are given by the projection of f_{j+1} onto the scaling functions $\varphi_{j,k}$:

$$\lambda_{j,k} = \int_{S^2} f_{j+1}(\omega)\ \varphi_{j,k}(\omega)\ \mathrm{d}\Omega\ .$$

- Detail coefficients at level j are given by the projection of f_{j+1} onto the wavelets $\psi^m_{j,k}$:

$$\gamma^m_{j,k} = \int_{S^2} f_{j+1}(\omega)\ \psi^m_{j,k}(\omega)\ \mathrm{d}\Omega\ .$$

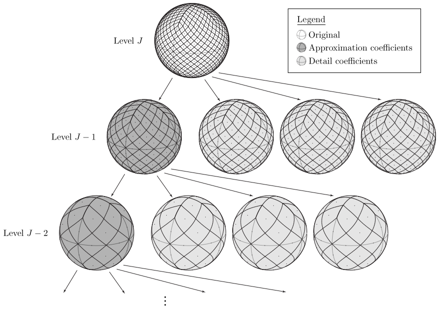

Figure: Haar multiresolution decomposition

- The function $f_J \in V_J$ may then be synthesised from its approximation and detail coefficients:

$$f_J(\omega) = \sum_{k=0}^{N_{J_0}-1} \lambda_{J_0 k}\varphi_{J_0 k}(\omega) + \sum_{j=J_0}^{J-1}\sum_{k=0}^{N_j-1}\sum_{m=0}^{2} \gamma^m_{j,k}\psi^m_{j,k}(\omega)\ .$$

Haar wavelets on the sphere

- Multiresolution decomposition of a function defined on a HEALPix data-sphere at resolution J, *i.e.* $f_J \in V_J$ proceeds as follows.
- Approximation coefficients at the coarser level j are given by the projection of f_{j+1} onto the scaling functions $\varphi_{j,k}$:

$$\lambda_{j,k} = \int_{S^2} f_{j+1}(\omega)\ \varphi_{j,k}(\omega)\ \mathrm{d}\Omega\ .$$

- Detail coefficients at level j are given by the projection of f_{j+1} onto the wavelets $\psi^m_{j,k}$:

$$\gamma^m_{j,k} = \int_{S^2} f_{j+1}(\omega)\ \psi^m_{j,k}(\omega)\ \mathrm{d}\Omega\ .$$

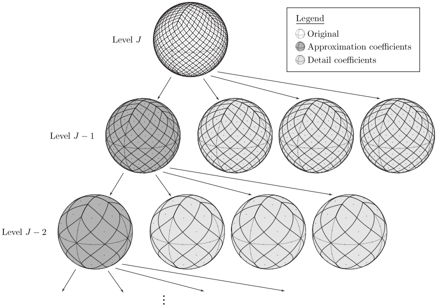

Figure: Haar multiresolution decomposition

- The function $f_J \in V_J$ may then be synthesised from its approximation and detail coefficients:

$$f_J(\omega) = \sum_{k=0}^{N_{J_0}-1} \lambda_{J_0 k}\varphi_{J_0 k}(\omega) + \sum_{j=J_0}^{J-1}\sum_{k=0}^{N_j-1}\sum_{m=0}^{2} \gamma^m_{j,k}\psi^m_{j,k}(\omega)\ .$$

Outline

Bubble universes

- In collaboration with: Stephen Feeney, Matthew Johnson, Daniel Mortlock & Hiranya Peiris (see Feeney *et al.* (2011a,2011b))
- Inflation: period of exponential expansion in the very early Universe, invoked to solve many fine-tuning problems.
- Strong observational evidence for inflation.

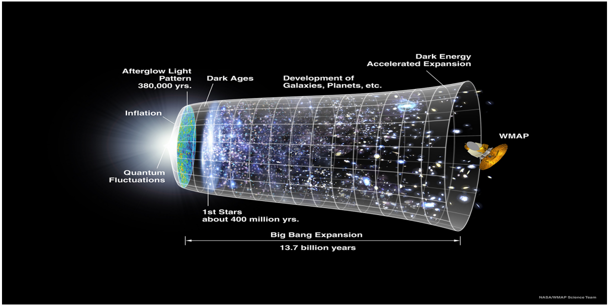

Bubble universes

- In collaboration with: Stephen Feeney, Matthew Johnson, Daniel Mortlock & Hiranya Peiris (see Feeney *et al.* (2011a,2011b))
- Inflation: period of exponential expansion in the very early Universe, invoked to solve many fine-tuning problems.
- Strong observational evidence for inflation.

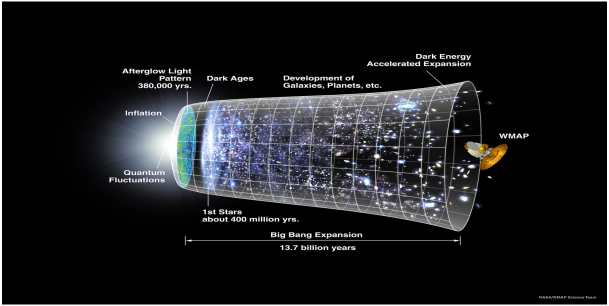

Slow-roll inflation

- Standard/simplest descriptions of inflation are slow-roll.
- However, this is a phenomenological description only and is not well motivated.
- We would like inflation to be a consequence of high-energy physics!

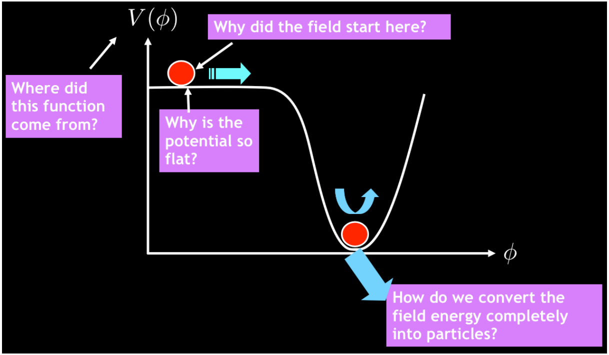

Slow-roll inflation

- Standard/simplest descriptions of inflation are slow-roll.
- However, this is a phenomenological description only and is not well motivated.
- **We would like inflation to be a consequence of high-energy physics!**

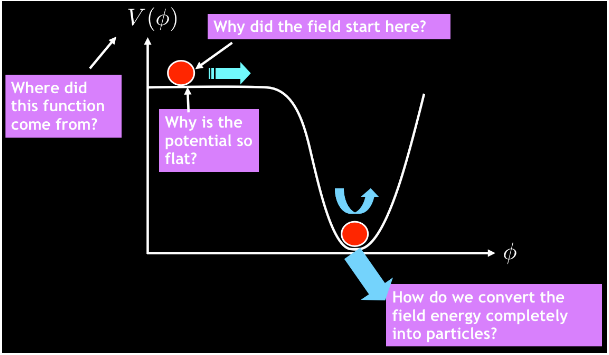

Eternal inflation

- Theories of inflation with a unique vacuum are difficult to come by.
- For example, string theories give landscape of 4D vacua, all of which are occupied.
- Field trapped in false vacuum $\Rightarrow$ inflates forever!

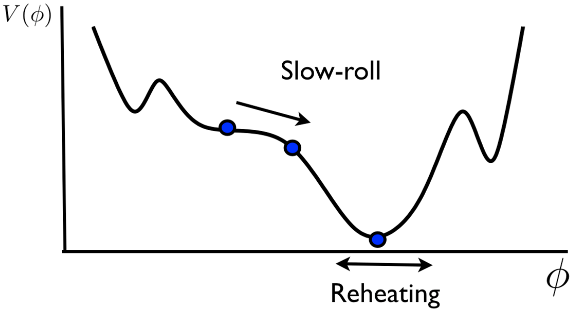

Eternal inflation

- Theories of inflation with a unique vacuum are difficult to come by.
- For example, string theories give landscape of 4D vacua, all of which are occupied.
- Field trapped in false vacuum $\Rightarrow$ inflates forever!
- Tunnelling creates a bubble!
- If bubble nucleation rate less than bulk expansion, then inflation is eternal.

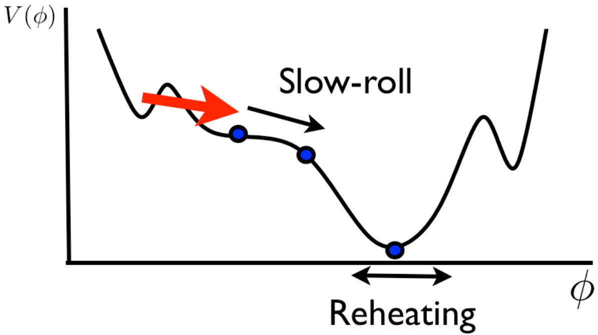

Eternal inflation

- Theories of inflation with a unique vacuum are difficult to come by.
- For example, string theories give landscape of 4D vacua, all of which are occupied.
- Field trapped in false vacuum $\Rightarrow$ inflates forever!
- Tunnelling creates a bubble!
- If bubble nucleation rate less than bulk expansion, then inflation is eternal.

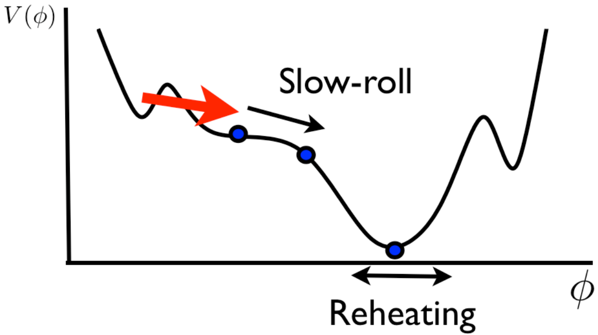

The Multiverse

The Multiverse

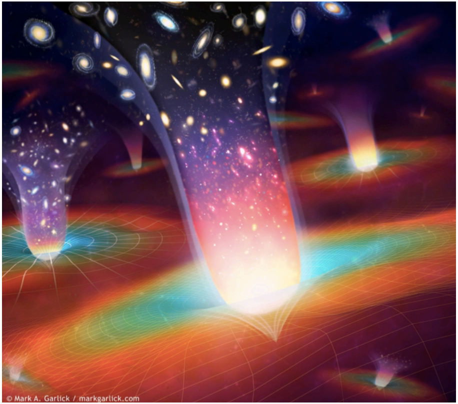

Bubble universes

(bubble movie)

[Credit: Anthony Aguirre]

Bubble collisions

- Bubble collisions may have left observational signatures in the CMB.

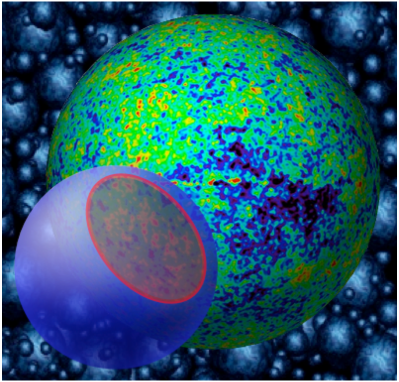

Bubble collisions

- Bubble collisions may have left observational signatures in the CMB.

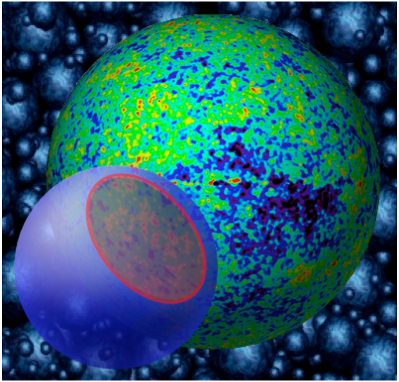

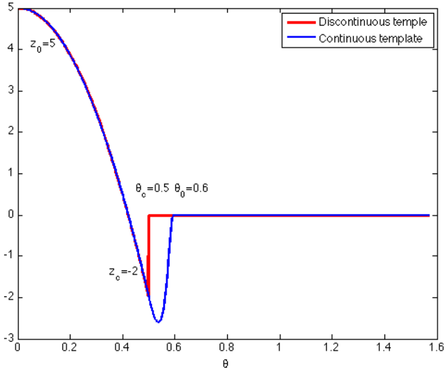

Full-sky object detection

- Bayesian objection detection would provide a rigorous statistical framework for comparing models with differing numbers of bubble collisions.
- However, such an analysis is computationally intractable!
  - Requires the inversion of a **3 million** $\times$ **3 million** matrix for WMAP data.
  - Requires the inversion of a **50 million** $\times$ **50 million** matrix for Planck data.
- Alternatively, perform a preprocessing to detect candidate bubble collisions, followed by a local Bayesian analysis.
- This approach has been pioneered by Feeney *et al.* (2011a,2011b), using wavelets (needlets) on the sphere.
- However, we know signature of candidate bubble collisions $\rightarrow$ exploit this knowledge!
- Build optimal filters tailored to the expected bubble collision signatures.
- Replace the wavelet (needlet) preprocessing stage with optimal filters.

Full-sky object detection

- Bayesian objection detection would provide a rigorous statistical framework for comparing models with differing numbers of bubble collisions.
- However, such an analysis is computationally intractable!
  - Requires the inversion of a **3 million** $\times$ **3 million** matrix for WMAP data.
  - Requires the inversion of a **50 million** $\times$ **50 million** matrix for Planck data.
- Alternatively, perform a preprocessing to detect candidate bubble collisions, followed by a local Bayesian analysis.
- This approach has been pioneered by Feeney *et al.* (2011a,2011b), using wavelets (needlets) on the sphere.
- However, we know signature of candidate bubble collisions $\rightarrow$ exploit this knowledge!
- Build optimal filters tailored to the expected bubble collision signatures.
- Replace the wavelet (needlet) preprocessing stage with optimal filters.

Full-sky object detection

- Bayesian objection detection would provide a rigorous statistical framework for comparing models with differing numbers of bubble collisions.
- However, such an analysis is computationally intractable!
  - Requires the inversion of a **3 million** $\times$ **3 million** matrix for WMAP data.
  - Requires the inversion of a **50 million** $\times$ **50 million** matrix for Planck data.
- Alternatively, perform a preprocessing to detect candidate bubble collisions, followed by a local Bayesian analysis.
- This approach has been pioneered by Feeney *et al.* (2011a,2011b), using wavelets (needlets) on the sphere.
- However, we know signature of candidate bubble collisions $\rightarrow$ exploit this knowledge!
- Build optimal filters tailored to the expected bubble collision signatures.
- Replace the wavelet (needlet) preprocessing stage with optimal filters.

Full-sky object detection

- Bayesian objection detection would provide a rigorous statistical framework for comparing models with differing numbers of bubble collisions.
- However, such an analysis is computationally intractable!
  - Requires the inversion of a **3 million** $\times$ **3 million** matrix for WMAP data.
  - Requires the inversion of a **50 million** $\times$ **50 million** matrix for Planck data.
- Alternatively, perform a preprocessing to detect candidate bubble collisions, followed by a local Bayesian analysis.
- This approach has been pioneered by Feeney *et al.* (2011a,2011b), using wavelets (needlets) on the sphere.
- However, we know signature of candidate bubble collisions $\rightarrow$ exploit this knowledge!
- Build optimal filters tailored to the expected bubble collision signatures.
- Replace the wavelet (needlet) preprocessing stage with optimal filters.

Filtering for full-sky object detection

- The observed field may be represented by

$$y(\omega) = \sum_i s_i(\omega) + n(\omega) \ .$$

- Each source may be represented in terms of its amplitude A_i and source profile:

$$s_i(\omega) = A_i \ \tau_i(\omega)$$

where $\tau_i(\omega)$ is a dilated and rotated version of the source profile $\tau(\omega)$ of default dilation centred on the north pole, *i.e.* $\tau_i(\omega) = \mathcal{R}(\rho_i)\mathcal{D}(R_i|p) \ \tau(\omega)$.

- One wishes to recover the parameters $\{A_i, R_i, \rho_i\}$ that describe each source amplitude, scale and position/orientation respectively.
- Filter the signal on the sphere to enhance the source profile relative to the background noise process $n(\omega)$:

$$\boxed{w(\rho, R|p) = \int_{S^2} f(\omega) \ [\mathcal{R}(\rho)\Psi_{R|p}]^*(\omega) \ \mathrm{d}\Omega(\omega) \ ,}$$

where $\Psi \in L^2(S^2, \ \mathrm{d}\Omega(\omega))$ is the filter kernel and p denotes the p-norm that the scaling R is defined to perserve.

Filtering for full-sky object detection

- The observed field may be represented by

$$y(\omega) = \sum_i s_i(\omega) + n(\omega) \ .$$

- Each source may be represented in terms of its amplitude A_i and source profile:

$$s_i(\omega) = A_i \ \tau_i(\omega)$$

where $\tau_i(\omega)$ is a dilated and rotated version of the source profile $\tau(\omega)$ of default dilation centred on the north pole, *i.e.* $\tau_i(\omega) = \mathcal{R}(\rho_i)\mathcal{D}(R_i|p) \ \tau(\omega)$.

- One wishes to recover the parameters $\{A_i, R_i, \rho_i\}$ that describe each source amplitude, scale and position/orientation respectively.

- Filter the signal on the sphere to enhance the source profile relative to the background noise process $n(\omega)$:

$$\boxed{w(\rho, R|p) = \int_{\mathrm{S}^2} f(\omega) \ [\mathcal{R}(\rho)\Psi_{R|p}]^*(\omega) \ \mathrm{d}\Omega(\omega) \ ,}$$

where $\Psi \in L^2(\mathrm{S}^2, \ \mathrm{d}\Omega(\omega))$ is the filter kernel and p denotes the p-norm that the scaling R is defined to perserve.

Filtering for full-sky object detection

- The observed field may be represented by

$$y(\omega) = \sum_i s_i(\omega) + n(\omega) \ .$$

- Each source may be represented in terms of its amplitude A_i and source profile:

$$s_i(\omega) = A_i \ \tau_i(\omega)$$

 where $\tau_i(\omega)$ is a dilated and rotated version of the source profile $\tau(\omega)$ of default dilation centred on the north pole, *i.e.* $\tau_i(\omega) = \mathcal{R}(\rho_i)\mathcal{D}(R_i|p) \ \tau(\omega)$.

- One wishes to recover the parameters $\{A_i, R_i, \rho_i\}$ that describe each source amplitude, scale and position/orientation respectively.

- Filter the signal on the sphere to enhance the source profile relative to the background noise process $n(\omega)$:

$$\boxed{w(\rho, R|p) = \int_{\mathrm{S}^2} f(\omega) \ [\mathcal{R}(\rho)\Psi_{R|p}]^*(\omega) \ \mathrm{d}\Omega(\omega) \ ,}$$

where $\Psi \in L^2(\mathrm{S}^2, \ \mathrm{d}\Omega(\omega))$ is the filter kernel and p denotes the p-norm that the scaling R is defined to perserve.

Matched filter (MF)

- Matched filtering has been considered extensively in Euclidean space (*e.g.* the plane) to enhance a source profile in a background noise process (*e.g.* Sanz *et al.* (2001), Herranz *et al.* (2002)).
- Extend matching filtering to the sphere (JDM *et al.* (2008)).

Matched filter (MF) on the sphere

The optimal MF defined on the sphere is obtained by solving the constrained optimisation problem:

$$\min_{\text{w.r.t. } (\Psi_{R|p})_{\ell m}} \sigma_w^2(\mathbf{0}, R|p) \qquad \text{such that} \qquad \langle w(\mathbf{0}, R|p) \rangle = A \ .$$

The spherical harmonic coefficients of the resultant MF are given by

$$\boxed{(\Psi_{R|p})_{\ell m} = \frac{\tau_{\ell m}}{a\, C_\ell} \ ,}$$

where

$$a = \sum_{\ell m} C_\ell^{-1} |\tau_{\ell m}|^2 \ .$$

Scale adaptive filter (SAF)

- Scale adaptive filter derived in Euclidean space by Sanz *et al.* (2001) and Herranz *et al.* (2002), not only to enhance the source profile, but also to impose an extreme in scale.
- Extended to the sphere (JDM *et al.* (2008)).

Scale adaptive filter (SAF) on the sphere

The optimal SAF defined on the sphere is obtained by by solving the constrained optimisation problem:

$$\min_{\text{w.r.t. } (\Psi_{R_0|p})_{\ell m}} \sigma_w^2(\mathbf{0}, R|p)$$

such that

$$\langle w(\mathbf{0}, R|p)\rangle = A \text{ and } \frac{\partial}{\partial R}\langle w(\mathbf{0}, R|p)\rangle\Big|_{R=R_0} = 0 \,.$$

The spherical harmonic coefficients of the resultant SAF are given by

$$\boxed{(\Psi_{R_0|p})_{\ell m} = \frac{c\tau_{\ell m} - b(A_{\ell p}\tau_{\ell m} - B_{\ell m}\tau_{\ell-1,m})}{\Delta C_\ell} \,,}$$

where

$$b = \sum_{\ell m} C_\ell^{-1}\tau_{\ell m}(A_{\ell p}\tau^*_{\ell m} - B_{\ell m}\tau^*_{\ell-1,m}) \,,$$

$$c = \sum_{\ell m} C_\ell^{-1}\left|A_{\ell p}\tau_{\ell m} - B_{\ell m}\tau_{\ell-1,m}\right|^2 \,,$$

$\Delta = ac - |b|^2$, a is defined as before, $A_{\ell p} \equiv \ell + 2/p - 1$ and $B_{\ell m} \equiv (\ell^2 - m^2)^{1/2}$.

Optimal filters for bubble signatures

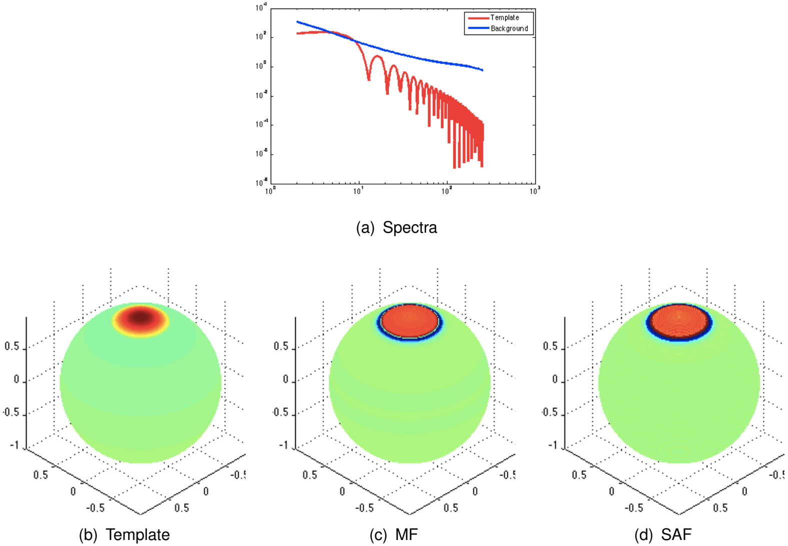

Figure: Optimal filters for bubble template with size $\theta_{\text{crit}} = 20°$.

Optimal filters for bubble signatures

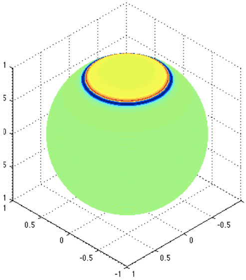

(a) $\theta_{\text{crit}} = 30^{\circ}$

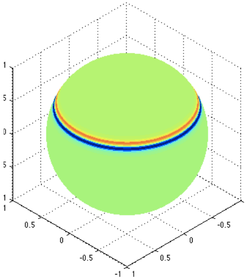

(b) $\theta_{\text{crit}} = 60^{\circ}$

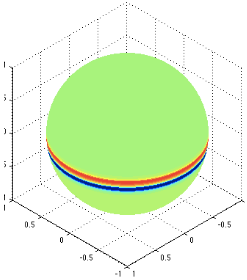

(c) $\theta_{\text{crit}} = 90^{\circ}$

Figure: MF for various template sizes

Theoretical signal-to-noise ratios (SNRs)

- Predict the expected SNR for a given filter:

$$\Gamma \equiv \frac{\langle w(\mathbf{0}, R|p)\rangle}{\sigma_w(\mathbf{0}, R|p)} \ .$$

- For the MF, SAF and any a arbitrary filter Ψ we find, respectively,

$$\Gamma_{\rm MF} = a^{1/2} A \ ,$$

$$\Gamma_{\rm SAF} = c^{-1/2} \Delta^{1/2} A \ ,$$

and

$$\Gamma_{\Psi} = \frac{A \sum_{\ell m} \tau_{\ell m} \Psi^*_{\ell m}}{\sqrt{\sum_{\ell m} C_\ell \left|\Psi_{\ell m}\right|^2}} \ .$$

- We can also predict the expected SNR of the unfiltered field:

$$\Gamma_{\rm orig} = \frac{A \sum_{\ell m} \sqrt{\frac{2\ell+1}{4\pi} \frac{(\ell-m)!}{(\ell+m)!}} \ \tau_{\ell m}}{\sqrt{\sum_\ell \frac{2\ell+1}{4\pi} C_\ell}} \ .$$

Theoretical signal-to-noise ratios (SNRs)

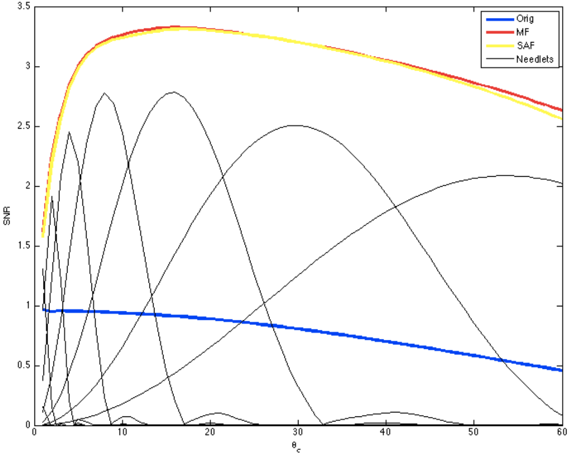

Figure: Theoretical SNRs versus template size $\theta_{\rm crit}$.

Detection algorithm for bubble signatures of unknown size

- Consider a discrete set of candidate θ_{crit} scales.
- Ensure grid sufficiently coarse that SNR not significantly hampered.

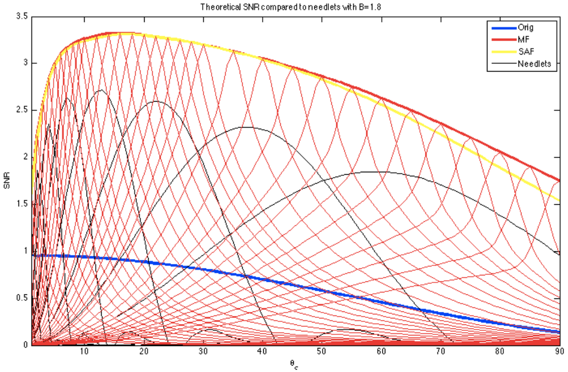

Figure: Theoretical SNRs for filters matched to given scale θ'_{crit}.

Detection algorithm for bubble signatures of unknown size

Bubble collision detection algorithm

1. Filter the sky with the matched filter for each scale (i.e. for each candidate $\theta_{\rm crit}$).
2. Compute significance maps for each filter scale, where the significance is given by the number of standard deviations that the filtered field deviates from the mean (3,000 Gaussian CMB simulations are used to determined the filtered field mean and variance).
3. Threshold the significance maps for each filter scale (the N_σ threshold for each filter will subsequently be calibrated from WMAP end-to-end simulations).
4. Find localised peaks in the thresholded significance maps for each filter scale.
5. Consider the local peak found at each scale. Look across adjacent scales and if a nearby region in an adjacent scale has a greater peak in the filtered field, then discard the current local peak. Otherwise retain the local peak as a detected source.
6. For all detected sources, estimate parameters of the source size, location and amplitude from the filter scale, peak position of the significance map and amplitude of the filtered field respectively.

Detection algorithm for bubble signatures of unknown size

Bubble collision detection algorithm

1. Filter the sky with the matched filter for each scale (i.e. for each candidate θ_{crit}).
2. Compute significance maps for each filter scale, where the significance is given by the number of standard deviations that the filtered field deviates from the mean (3,000 Gaussian CMB simulations are used to determined the filtered field mean and variance).
3. Threshold the significance maps for each filter scale (the N_σ threshold for each filter will subsequently be calibrated from WMAP end-to-end simulations).
4. Find localised peaks in the thresholded significance maps for each filter scale.
5. Consider the local peak found at each scale. Look across adjacent scales and if a nearby region in an adjacent scale has a greater peak in the filtered field, then discard the current local peak. Otherwise retain the local peak as a detected source.
6. For all detected sources, estimate parameters of the source size, location and amplitude from the filter scale, peak position of the significance map and amplitude of the filtered field respectively.

Detection algorithm for bubble signatures of unknown size

Bubble collision detection algorithm

1. Filter the sky with the matched filter for each scale (i.e. for each candidate $\theta_{\rm crit}$).
2. Compute significance maps for each filter scale, where the significance is given by the number of standard deviations that the filtered field deviates from the mean (3,000 Gaussian CMB simulations are used to determined the filtered field mean and variance).
3. Threshold the significance maps for each filter scale (the N_σ threshold for each filter will subsequently be calibrated from WMAP end-to-end simulations).
4. Find localised peaks in the thresholded significance maps for each filter scale.
5. Consider the local peak found at each scale. Look across adjacent scales and if a nearby region in an adjacent scale has a greater peak in the filtered field, then discard the current local peak. Otherwise retain the local peak as a detected source.
6. For all detected sources, estimate parameters of the source size, location and amplitude from the filter scale, peak position of the significance map and amplitude of the filtered field respectively.

Detection algorithm for bubble signatures of unknown size

Bubble collision detection algorithm

1. Filter the sky with the matched filter for each scale (i.e. for each candidate θ_{crit}).
2. Compute significance maps for each filter scale, where the significance is given by the number of standard deviations that the filtered field deviates from the mean (3,000 Gaussian CMB simulations are used to determined the filtered field mean and variance).
3. Threshold the significance maps for each filter scale (the N_σ threshold for each filter will subsequently be calibrated from WMAP end-to-end simulations).
4. Find localised peaks in the thresholded significance maps for each filter scale.
5. Consider the local peak found at each scale. Look across adjacent scales and if a nearby region in an adjacent scale has a greater peak in the filtered field, then discard the current local peak. Otherwise retain the local peak as a detected source.
6. For all detected sources, estimate parameters of the source size, location and amplitude from the filter scale, peak position of the significance map and amplitude of the filtered field respectively.

Detection algorithm for bubble signatures of unknown size

Bubble collision detection algorithm

1. Filter the sky with the matched filter for each scale (i.e. for each candidate $\theta_{\rm crit}$).
2. Compute significance maps for each filter scale, where the significance is given by the number of standard deviations that the filtered field deviates from the mean (3,000 Gaussian CMB simulations are used to determined the filtered field mean and variance).
3. Threshold the significance maps for each filter scale (the N_σ threshold for each filter will subsequently be calibrated from WMAP end-to-end simulations).
4. Find localised peaks in the thresholded significance maps for each filter scale.
5. Consider the local peak found at each scale. Look across adjacent scales and if a nearby region in an adjacent scale has a greater peak in the filtered field, then discard the current local peak. Otherwise retain the local peak as a detected source.
6. For all detected sources, estimate parameters of the source size, location and amplitude from the filter scale, peak position of the significance map and amplitude of the filtered field respectively.

Detection algorithm for bubble signatures of unknown size

Bubble collision detection algorithm

1. Filter the sky with the matched filter for each scale (i.e. for each candidate $\theta_{\rm crit}$).
2. Compute significance maps for each filter scale, where the significance is given by the number of standard deviations that the filtered field deviates from the mean (3,000 Gaussian CMB simulations are used to determined the filtered field mean and variance).
3. Threshold the significance maps for each filter scale (the N_σ threshold for each filter will subsequently be calibrated from WMAP end-to-end simulations).
4. Find localised peaks in the thresholded significance maps for each filter scale.
5. Consider the local peak found at each scale. Look across adjacent scales and if a nearby region in an adjacent scale has a greater peak in the filtered field, then discard the current local peak. Otherwise retain the local peak as a detected source.
6. For all detected sources, estimate parameters of the source size, location and amplitude from the filter scale, peak position of the significance map and amplitude of the filtered field respectively.

Detection algorithm illustrated

- Embed bubble signatures at sizes $\theta_{\rm crit}^{\rm truth} \in \{10^\circ, 13^\circ, 20^\circ\}$ but consider discretised grid of $\theta_{\rm crit} \in \{5^\circ, 10^\circ, 20^\circ, 30^\circ\}$.

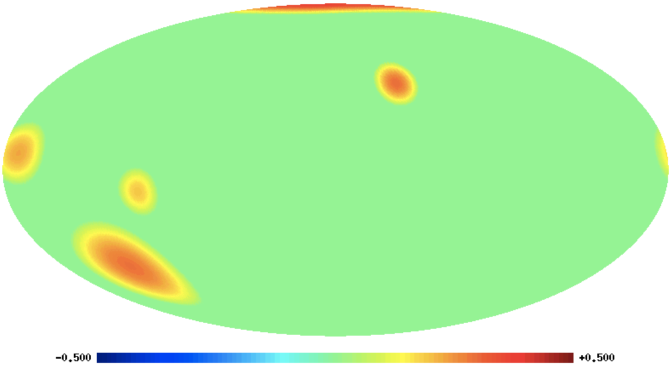

Figure: Embedded bubble collision signatures.

Detection algorithm illustrated

- Embed bubble signatures at sizes $\theta_{\rm crit}^{\rm truth} \in \{10^\circ, 13^\circ, 20^\circ\}$ but consider discretised grid of $\theta_{\rm crit} \in \{5^\circ, 10^\circ, 20^\circ, 30^\circ\}$.

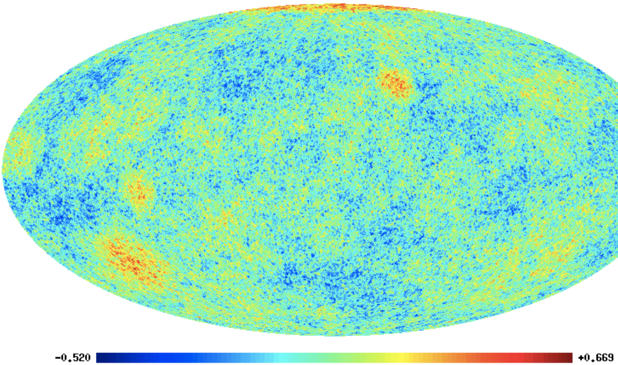

Figure: Simulated data.

Detection algorithm illustrated

- Embed bubble signatures at sizes $\theta_{\rm crit}^{\rm truth} \in \{10^\circ, 13^\circ, 20^\circ\}$ but consider discretised grid of $\theta_{\rm crit} \in \{5^\circ, 10^\circ, 20^\circ, 30^\circ\}$.

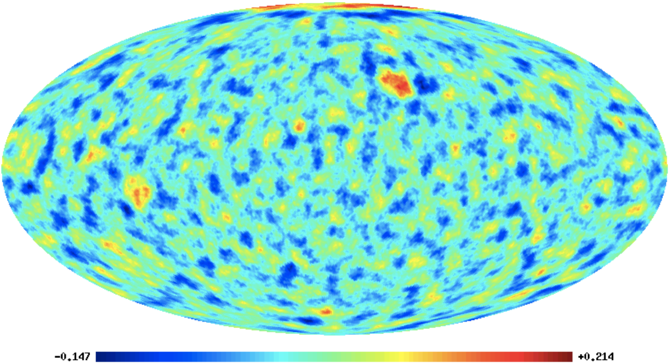

Figure: Filtered field for $\theta_{\rm crit} = 5^\circ$.

Detection algorithm illustrated

- Embed bubble signatures at sizes $\theta_{\text{crit}}^{\text{truth}} \in \{10^\circ, 13^\circ, 20^\circ\}$ but consider discretised grid of $\theta_{\text{crit}} \in \{5^\circ, 10^\circ, 20^\circ, 30^\circ\}$.

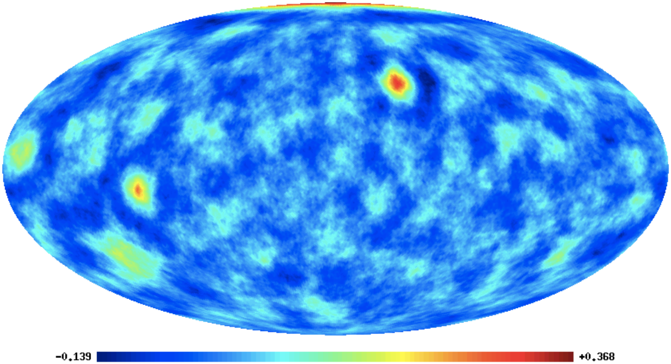

Figure: Filtered field for $\theta_{\text{crit}} = 10^\circ$.

Detection algorithm illustrated

- Embed bubble signatures at sizes $\theta_{\text{crit}}^{\text{truth}} \in \{10^\circ, 13^\circ, 20^\circ\}$ but consider discretised grid of $\theta_{\text{crit}} \in \{5^\circ, 10^\circ, 20^\circ, 30^\circ\}$.

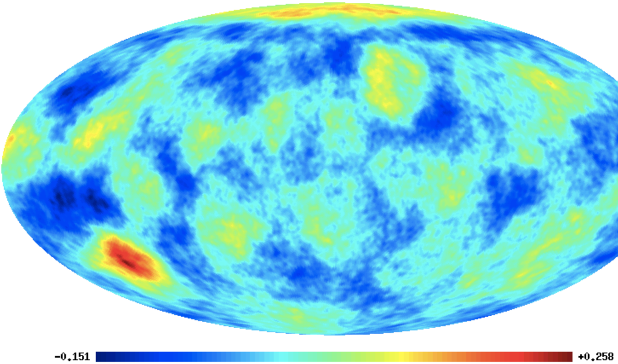

Figure: Filtered field for $\theta_{\text{crit}} = 20^\circ$.

Detection algorithm illustrated

- Embed bubble signatures at sizes $\theta_{\text{crit}}^{\text{truth}} \in \{10^\circ, 13^\circ, 20^\circ\}$ but consider discretised grid of $\theta_{\text{crit}} \in \{5^\circ, 10^\circ, 20^\circ, 30^\circ\}$.

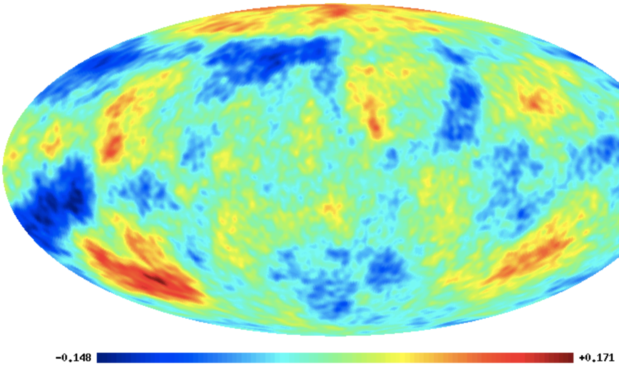

Figure: Filtered field for $\theta_{\text{crit}} = 30^\circ$.

Detection algorithm illustrated

- Embed bubble signatures at sizes $\theta_{\text{crit}}^{\text{truth}} \in \{10^\circ, 13^\circ, 20^\circ\}$ but consider discretised grid of $\theta_{\text{crit}} \in \{5^\circ, 10^\circ, 20^\circ, 30^\circ\}$.

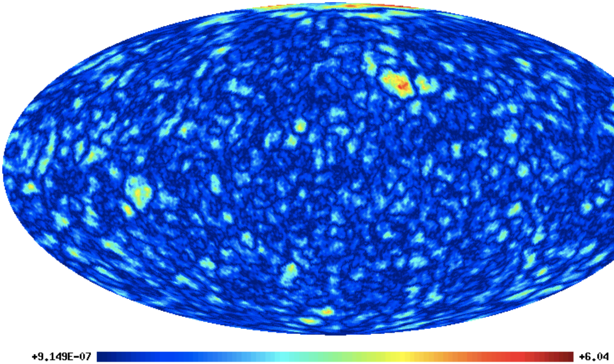

Figure: Significance map for $\theta_{\text{crit}} = 5^\circ$.

Detection algorithm illustrated

- Embed bubble signatures at sizes $\theta_{\rm crit}^{\rm truth} \in \{10^\circ, 13^\circ, 20^\circ\}$ but consider discretised grid of $\theta_{\rm crit} \in \{5^\circ, 10^\circ, 20^\circ, 30^\circ\}$.

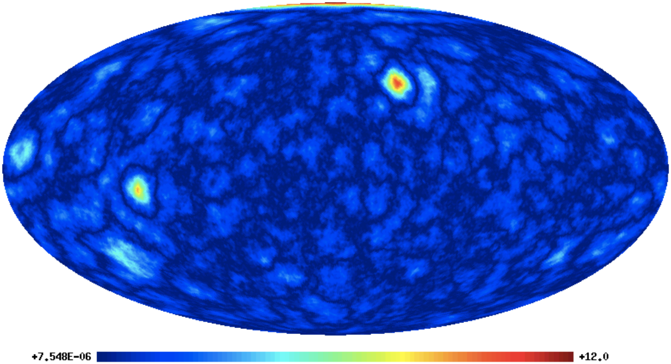

Figure: Significance map for $\theta_{\rm crit} = 10^\circ$.

Detection algorithm illustrated

- Embed bubble signatures at sizes $\theta_{\rm crit}^{\rm truth} \in \{10^\circ, 13^\circ, 20^\circ\}$ but consider discretised grid of $\theta_{\rm crit} \in \{5^\circ, 10^\circ, 20^\circ, 30^\circ\}$.

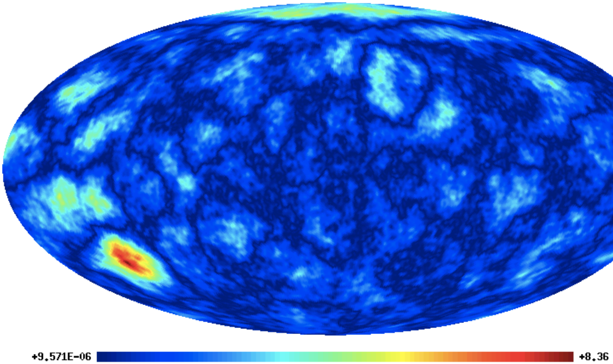

Figure: Significance map for $\theta_{\rm crit} = 20^\circ$.

Detection algorithm illustrated

- Embed bubble signatures at sizes $\theta_{\text{crit}}^{\text{truth}} \in \{10^\circ, 13^\circ, 20^\circ\}$ but consider discretised grid of $\theta_{\text{crit}} \in \{5^\circ, 10^\circ, 20^\circ, 30^\circ\}$.

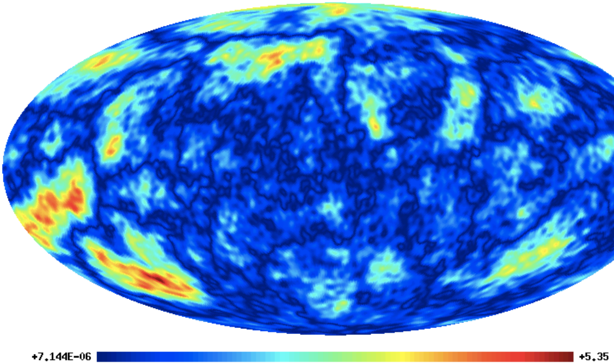

Figure: Significance map for $\theta_{\text{crit}} = 30^\circ$.

Detection algorithm illustrated

- Embed bubble signatures at sizes $\theta_{\text{crit}}^{\text{truth}} \in \{10^\circ, 13^\circ, 20^\circ\}$ but consider discretised grid of $\theta_{\text{crit}} \in \{5^\circ, 10^\circ, 20^\circ, 30^\circ\}$.

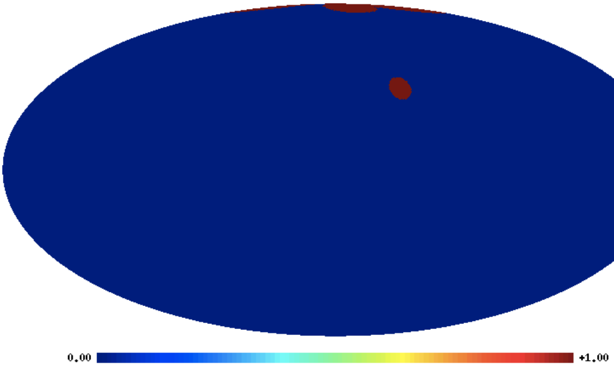

Figure: Detected regions for $\theta_{\text{crit}} = 5^\circ$.

Detection algorithm illustrated

- Embed bubble signatures at sizes $\theta_{\rm crit}^{\rm truth} \in \{10^\circ, 13^\circ, 20^\circ\}$ but consider discretised grid of $\theta_{\rm crit} \in \{5^\circ, 10^\circ, 20^\circ, 30^\circ\}$.

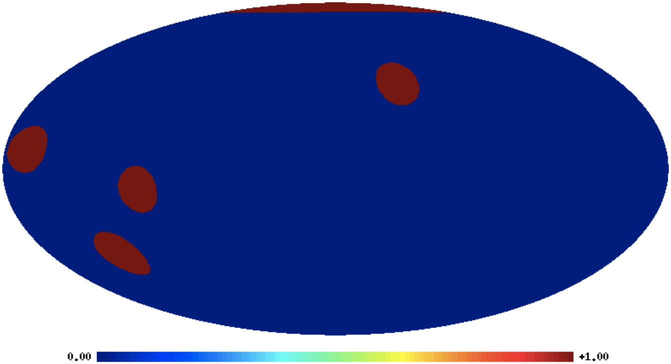

Figure: Detected regions for $\theta_{\rm crit} = 10^\circ$.

Detection algorithm illustrated

- Embed bubble signatures at sizes $\theta_{\text{crit}}^{\text{truth}} \in \{10^\circ, 13^\circ, 20^\circ\}$ but consider discretised grid of $\theta_{\text{crit}} \in \{5^\circ, 10^\circ, 20^\circ, 30^\circ\}$.

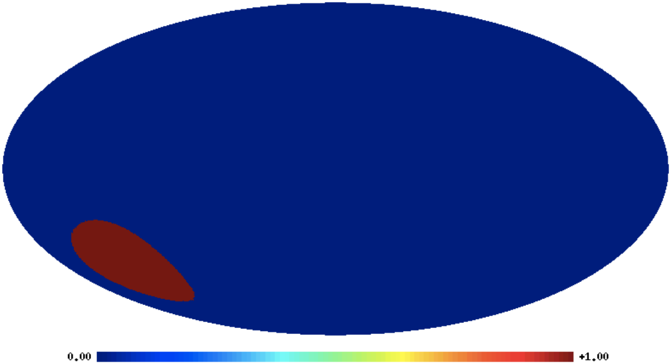

Figure: Detected regions for $\theta_{\text{crit}} = 20^\circ$.

Detection algorithm illustrated

- Embed bubble signatures at sizes $\theta_{\rm crit}^{\rm truth} \in \{10^\circ, 13^\circ, 20^\circ\}$ but consider discretised grid of $\theta_{\rm crit} \in \{5^\circ, 10^\circ, 20^\circ, 30^\circ\}$.

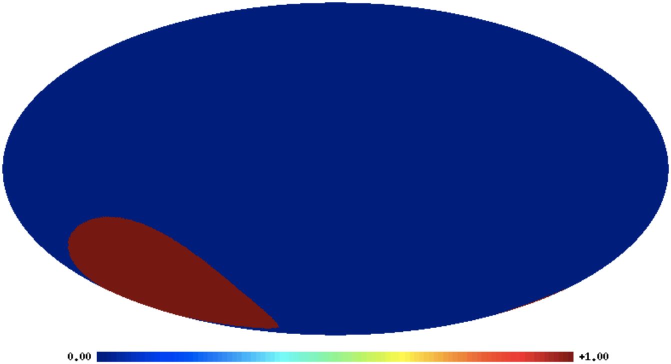

Figure: Detected regions for $\theta_{\rm crit} = 30^\circ$.

Detection algorithm illustrated

- Embed bubble signatures at sizes $\theta_{\rm crit}^{\rm truth} \in \{10^\circ, 13^\circ, 20^\circ\}$ but consider discretised grid of $\theta_{\rm crit} \in \{5^\circ, 10^\circ, 20^\circ, 30^\circ\}$.

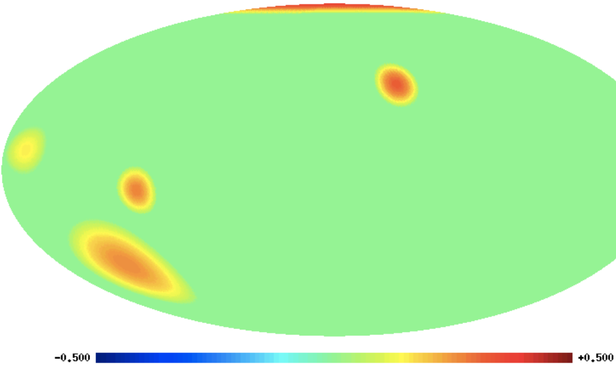

Figure: Detected regions.

Detection algorithm illustrated

- Embed bubble signatures at sizes $\theta_{\rm crit}^{\rm truth} \in \{10^\circ, 13^\circ, 20^\circ\}$ but consider discretised grid of $\theta_{\rm crit} \in \{5^\circ, 10^\circ, 20^\circ, 30^\circ\}$.

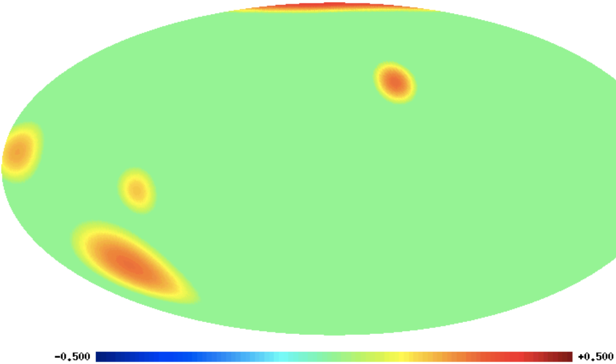

Figure: Ground truth.

Detection algorithm illustrated

- All objects detected successfully with no false detections (as expected for the intense bubble signatures considered in this illustration).
- Bubble collision template parameters estimated reasonably accurately for the preprocessing stage.
- Performed an extensive comparison and optimal filters found to be approximately twice as sensitive as needlets.

Source	Original size	Detected size	Original amplitude (mK)	Detected amplitude (mK)
1	10°	10°	0.34	0.36
2	10°	10°	0.30	0.31
3	13°	10°	0.23	0.15
4	10°	10°	0.19	0.24
5	20°	20°	0.29	0.25

Candidate bubble collisions in WMAP 7-year observations

- Applied candidate bubble collision detection algorithm to WMAP W-band 7-year data.
- First calibrated N_σ thresholds on WMAP end-to-end simulations (without bubble collisions), resulting in 13 false detections (allow a manageable number of false detections since preprocessing).

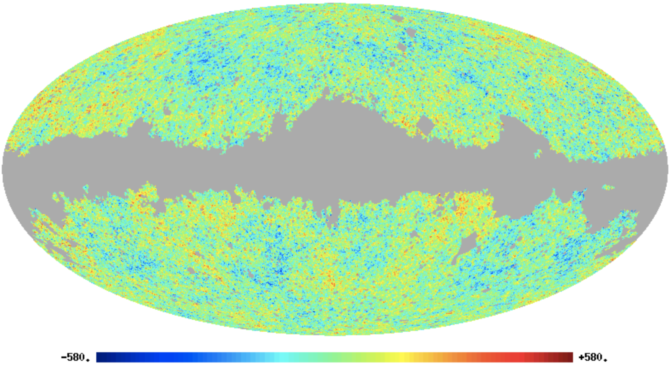

Figure: WMAP W-band 7-year data

Candidate bubble collisions in WMAP 7-year observations

- Applied candidate bubble collision detection algorithm to WMAP W-band 7-year data.
- First calibrated N_σ thresholds on WMAP end-to-end simulations (without bubble collisions), resulting in 13 false detections (allow a manageable number of false detections since preprocessing).

16 candidate bubble collisions detected in WMAP 7-year data for follow-up analysis (8 new regions not detected previously)!

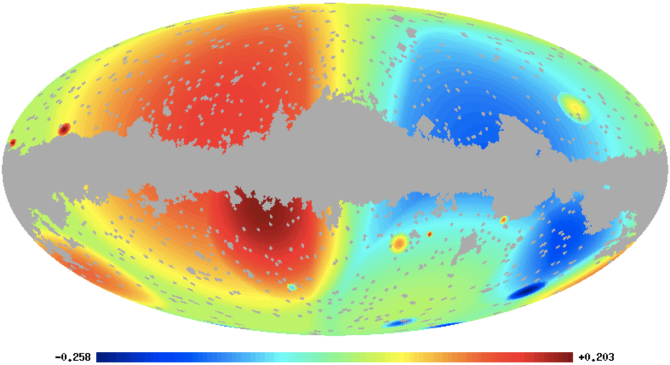

Figure: Candidate bubble collisions

Candidate bubble collisions in WMAP 7-year observations

- Applied candidate bubble collision detection algorithm to WMAP W-band 7-year data.
- First calibrated N_σ thresholds on WMAP end-to-end simulations (without bubble collisions), resulting in 13 false detections (allow a manageable number of false detections since preprocessing).

16 candidate bubble collisions detected in WMAP 7-year data for follow-up analysis (8 new regions not detected previously)!

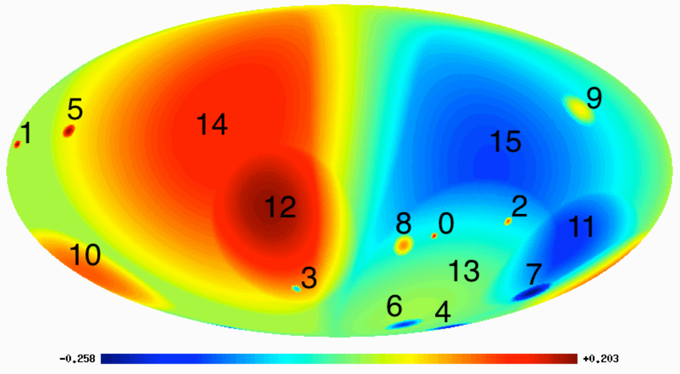

Figure: Candidate bubble collisions

Summary

- Although a general cosmological concordance model is now established, many details remain unclear.
- Cosmological signals are inherently observed on the celestial sphere
  $\rightarrow$ we must respect this geometry in any subsequent analysis.
- Developed new spherical signal processing methods, including: sampling theorems, wavelets, compressive sensing and optimal filters.
- The power of these techniques will help to unlock the secrets of the Universe.
- Detected potential observational signatures in the CMB of collisions between bubble universes.
- **First observational evidence for eternal inflation?**